Dissertationes Forestales 200

Towards an enhanced understanding of airborne LiDAR measurements of forest vegetation

Aarne Hovi

Department of Forest Sciences
Faculty of Agriculture and Forestry
University of Helsinki

Academic dissertation

To be presented with the permission of the Faculty of Agriculture and Forestry, University of Helsinki, for public criticism in the Ls 2 auditorium of the B-building (Latokartanonkaari 7) on September 25th, 2015, at 10 o'clock.

Title of dissertation: Towards an enhanced understanding of airborne LiDAR measurements of forest vegetation

Author: Aarne Hovi

Dissertationes Forestales 200

http://dx.doi.org/10.14214/df.200

Thesis supervisors:
Docent Ilkka Korpela
Department of Forest Sciences, University of Helsinki, Finland
Senior researcher Jari Vauhkonen
School of Forest Sciences, University of Eastern Finland

Pre-examiners:
Senior lecturer Mathias Disney
Department of Geography, University College London, UK
Associate professor Chris Hopkinson
Department of Geography, University of Lethbridge, Canada

Opponent:
Professor Juha Hyyppä
Department of Remote Sensing and Photogrammetry, Finnish Geospatial Research Institute

ISSN 1795-7389 (online)
ISBN 978-951-651-489-8 (pdf)

ISSN 2323-9220 (print)
ISBN 978-951-651-490-4 (paperback)

Publishers:
Finnish Society of Forest Science
Natural Resources Institute Finland
Faculty of Agriculture and Forestry of the University of Helsinki
School of Forest Sciences of the University of Eastern Finland

Editorial office:
Finnish Society of Forest Science
P.O. Box 18 FI-01301 Vantaa, Finland
http://www.metla.fi/dissertationes

Hovi, A. 2015. Towards an enhanced understanding of airborne LiDAR measurements of forest vegetation. Dissertationes Forestales 200. 69 p.
http://dx.doi.org/10.14214/df.200

ABSTRACT

This thesis presents basic research on how airborne LiDAR measurements of forest vegetation are influenced by the interplay of the geometric-optical properties of vegetation, sensor function and acquisition settings. Within the work, examining the potential of waveform (WF) recording sensors was of particular interest.

Study I focused upon discrete return LiDAR measurements of understory trees. It showed that transmission losses influenced the intensity of observations and echo triggering probabilities, and also skewed the distribution of echoes towards those triggered by highly reflective or dense targets. The intensity data were of low value for species identification, but the abundance of understory trees could be predicted based on echo height distributions.

In study II, a method of close-range terrestrial photogrammetry was developed. Images were shown as being useful for visualizations and even the geometric quality control of LiDAR data. The strength of backscattering was shown to correlate with the projected area extracted from the images.

In study III, a LiDAR simulation model was developed and validated against real measurements. The model was able to be used for sensitivity analyses to illustrate how plant structure or different pulse properties influence the WF data. Both simulated and real data showed that WF data were able to capture small-scale variations in the structural and optical properties of juvenile forest vegetation.

Study IV illustrated the potential of WF data in the species classification of larger trees. The WF features that separated tree species were also dependent on other variables such as tree size and phenology. Inherent between-tree differences in structure were quantified and the effects of pulse density on the features were examined.

Overall, the thesis provides basic findings on how LiDAR pulses interact with forest vegetation, and serves to link theory with real observations. The results contribute to an improved understanding of LiDAR measurements and their limitations, and thus provide support for further improvements in both data interpretation methods and specific sensor design.

Keywords: remote sensing, forest inventory, laser scanning, pulsed LiDAR, calibration, radiative transfer, ray tracing

ACKNOWLEDGEMENTS

I made the first measurements for this thesis in summer of 2009 when I was working as a research assistant in Hyytiälä. Since then I have been extremely lucky to have the opportunity to work with interesting research topics and projects, and to learn a lot about doing research. Without the help of all the people involved, this thesis would not have been possible in its present thoroughness and quality.

First of all, I want to thank my supervisor Ilkka Korpela, who successfully guided me through this project. He patiently transferred me his knowledge of photogrammetry and laser scanning, and organized the funding which enabled me to concentrate on this thesis. Over these years we have spent lots of time together discussing about research and also other things in life, particularly during the many field trips in Hyytiälä, from which I have lots of good memories. My second supervisor Jari Vauhkonen was always ready to comment and discuss my work and, since he was not directly working in the project, helped to look at the things from a different perspective. Lauri Korhonen was almost like a third supervisor and provided crucial help when I was writing study IV. I also want to thank professor Pauline Stenberg and the other supervisory team members Bo Dahlin and Markus Holopainen, who all had a friendly and warm attitude towards me and always provided support if I needed. Special thanks to Pauline and Markus for letting me participate in teaching in their courses. The studies in the thesis attained their present form through the input from all co-authors. In addition to Ilkka, Jari, and Lauri, I owe gratitude to Felix Morsdorf who co-authored in study I.

This work was conducted at University of Helsinki in the Department of Forest Sciences. I want to thank all colleagues there and elsewhere for their scientific support, technical assistance, and discussions. I do not even try to list all of you by name, but each and every one of you made your important contribution to this thesis.

The studies required lots of data. In addition to people already mentioned, Harri Hytönen, Juha Inkilä, Laura Kakkonen, Timo Ketolainen, Pauliina Kulha, Petr Lukeš, and many forestry students participated in the field data collection. Staff at Hyytiälä Forestry Field Station provided help in arranging the field campaigns. People at Finnmap FM-international patiently helped with LiDAR data processing. Office staff in Viikki ensured that practical things were running smoothly.

Finally, I want to thank my friends and family who helped me to relax in free time and ensured that there were also many other things than science that enriched my life.

Majority of this thesis work was conducted under the Academy of Finland project ‘*Timestamped and free photons — quantitative airborne remote sensing of forests*’. Grants for visiting international conferences were obtained from Suomen Metsätieteellinen Seura and University of Helsinki. Many of the data items that I used were collected already long before I started to work on this thesis. The remote sensing experimentation in Hyytiälä has been maintained with the help of labor input and financial support by numerous people, institutions, and companies. All of them made this work possible.

Helsinki, August 2015

Aarne Hovi

LIST OF ORIGINAL ARTICLES

This thesis is based on the following research articles, which are referred to in the text by their Roman numerals. Articles I–III are reprinted with the permission of the publishers. Article IV is an author version of a manuscript accepted for publication.

I Korpela I., Hovi A., Morsdorf F. (2012). Understory trees in airborne LiDAR data - Selective mapping due to transmission losses and echo-triggering mechanisms. Remote Sensing of Environment 119: 92–104.
http://dx.doi.org/10.1016/j.rse.2011.12.011

II Korpela I., Hovi A., Korhonen L. (2013). Backscattering of individual LiDAR pulses explained by photogrammetrically derived vegetation structure. ISPRS Journal of Photogrammetry and Remote Sensing 83: 81–93.
http://dx.doi.org/10.1016/j.isprsjprs.2013.06.002

III Hovi A., Korpela I. (2014). Real and simulated waveform-recording LiDAR data in juvenile boreal forest vegetation. Remote Sensing of Environment 140: 665–678.
http://dx.doi.org/10.1016/j.rse.2013.10.003

IV Hovi A., Korhonen L., Vauhkonen J., Korpela I. (2015). LiDAR waveform features for tree species classification and their sensitivity to tree- and acquisition related parameters. Manuscript accepted for publication in Remote Sensing of Environment.
http://dx.doi.org/10.1016/j.rse.2015.08.019

Contributions:

(I) Hovi lead the field work, conducted the data analyses and shared an equal part in writing with Korpela. Korpela developed the idea, planned the experiment and was the main author. Morsdorf provided advice in radiative transfer theory and commented on the manuscript.

(II) Hovi participated in the field work, photogrammetry and in writing the paper. Korpela planned the experiment, conducted the data analyses and was the main author with responsibility for writing the photogrammetric section of the paper. The coverage of LiDAR theory was authored by Hovi. Korhonen assisted in the planning and writing phases of the article.

(III) Hovi was the main author, planned the study with Korpela, wrote the ray-tracing LiDAR simulator program, developed the geometric-optical plant models and conducted the analyses. Korpela participated in the planning and writing phases of the article.

(IV) Hovi was the main author and planned the analyses with Korpela and Vauhkonen. Korhonen provided help in structuring the manuscript and refining the analyses in the writing phase. All co-authors commented on the manuscript.

TABLE OF CONTENTS

SYMBOLS AND ABBREVIATIONS

A	Peak amplitude (of a NEAS)
A/D	Analogue to digital
AGC	Automatic gain control
ALS	Airborne laser scanning
BRDF	Bi-directional reflectance distribution function
BRF	Bi-directional reflectance factor
BTDF	Bi-directional transmittance distribution function
CFD	Constant fraction discriminator
d_{13}	Diameter at breast height, m
DR	Discrete return
E	Energy (NEAS)
EO	Exterior orientation
$EQ50$	Center of gravity (NEAS)
FWHM	Full width at half maximum, nanoseconds
$FWHM$	Full width at half maximum (NEAS), nanoseconds
GNSS	Global navigation satellite system
h	Height, m
HDRF	Hemispherical-directional reflectance factor
I	Intensity (of a DR echo)
iFOV	Instantaneous field of view
IMU	Inertial measurement unit
IO	Interior orientation
L	Length (NEAS), nanoseconds
λ	Wavelength, m
LAI	Leaf area index
LiDAR	Light detection and ranging
LME	Linear mixed-effects model
MCRT	Monte-Carlo ray tracing
NEAS	Noise-exceeding amplitude sequence
N_{peaks}	Number of peaks (NEAS)
NIR	Near infrared ($\lambda = 0.7$–1.35 μm)
PRF	Pulse repetition frequency, kHz
R	Scanning range, m
SD	Standard deviation
SNR	Signal to noise ratio, dB
SWIR	Shortwave infrared ($\lambda = 1.35$–2.7 μm)
TLS	Terrestrial laser scanning
WF	Waveform

1 INTRODUCTION

1.1 Background

LiDAR (Light Detection and Ranging) is an active remote sensing (RS) technology. LiDAR sensors perform distance measurements with beams of emitted laser light (Petrie and Toth 2009). Airborne LiDAR provides high resolution 3D information about vegetation and ground topography, and is therefore well-suited for forest vegetation mapping. LiDAR measures tree heights and canopy cover almost directly, whereas tree volume or biomass can be predicted using indirect estimation techniques (Lim et al. 2003).

Research into the use of LiDAR in forestry started with profiling instruments in the late 1970s (for a review, see Nelson 2013). The real breakthrough came in the late 1990s in the form of pulsed sensors, which materialized the advances made in direct georeferencing, scanning mechanisms, pulse repetition rate and increased laser power that enabled efficient wall-to-wall mapping with high spatial resolution using high-altitude airborne laser scanning (ALS) (Lim et al 2003; Næsset et al. 2004). The first studies reported on the use of ALS data for the estimation of canopy heights (Nilsson 1996; Næsset 1997a; Magnussen and Boudewyn 1998; Means et al. 1999) and basal area, biomass or stem volume (Nilsson 1996; Næsset 1997b; Lefsky et al. 1999; Means et al. 1999). The commercial sensors which were used followed the small-footprint discrete return (DR) design, while large-footprint waveform (WF) recording sensors were only in experimental use (Lim et al. 2003). Small-footprint DR sensors were well suited to topographic applications. These became the main commercial sensor type and were used in the ALS-based forest management planning inventories that became operational in the Nordic countries around 8−10 years ago (Næsset et al. 2004; Maltamo and Packalén 2014). DR sensors provide important point clouds almost directly. Small-footprint WF sensors have gained a foothold in markets over recent years, although most customers need point clouds for their applications and the post processing software for WF data is scarce. Owing to the fact that the shapes of the transmitted and received pulse are stored, it can be argued that WF sensors provide a more transparent view of the measurement process, and this is therefore beneficial for the better understanding and modeling of LiDAR measurements (Roncat et al. 2014b).

The forestry applications of small-footprint LiDAR data include medium-scale forest management planning inventories, large-scale multi-phase inventories with a sampling design, change mapping and monitoring, as well as the inventory of ecologically important variables such as biomass, canopy cover, leaf area index (LAI), or the presence of dead wood (Vauhkonen et al. 2014a). The inventory results form an output that is used for decision-making, which may realize benefits. The cost-efficiency of an inventory can be improved either by reducing costs, or by improving the quality of the inventory product to enable optimal decision making. The costs of ALS data acquisition can be reduced by using higher flying altitudes, fast flying speeds, and employing sensors that reach a high pulse repetition frequency (PRF) without compromising the signal-to-noise ratio (SNR). The post processing of data should be as automatic as possible. Costs related to the collection of training and validation field data form the main budget expenditure item of many applications. However, they can be reduced by developing the interpretation algorithms which are used and designing optimized sensors for a given task. Algorithm and sensor development also improves the quality of the inventory product. The need for a thorough understanding of the physical linkage between vegetation variables and the LiDAR signal has been addressed by several authors (Lim et al. 2003; Wulder et al. 2013; Roncat et al. 2014b), and this could contribute to the development of both data interpretation algorithms and sensors (Lim et al. 2003; Disney et al. 2010; Roncat et al. 2014b).

This thesis focuses mainly on basic research surrounding pulse-vegetation interactions, with a general objective of improving the state-of-the-art understanding of LiDAR measurements. Thus, the thesis is not confined to any particular application. Work on the thesis began soon after the compartment and mean-tree based forest management planning inventory system (Poso 1983) had been replaced by a LiDAR-assisted system that also uses aerial images as auxiliary information (Maltamo and Packalén 2014). The inventory results and management proposals are still presented for compartments, as this reflects the current silvicultural practice in Finland. Some tasks are still defined as forming bottleneck areas in the LiDAR-based system. Whilst these provided the rationales behind the individual studies of the thesis, a detailed discussion of them is largely omitted in the introduction.

The next sections elaborate the LiDAR measurement process and summarize the state-of-the-art understanding in pulse-vegetation interactions, thus giving the reader the necessary background information for the sections that follow. The rationales and objectives of the thesis are listed at the end of the Introduction.

1.2 LiDAR systems and data acquisition

1.2.1 LiDAR systems and geometric calibration

A LiDAR system is composed of a platform, a stabilized mount, the position and orientation system (GNSS, IMU), and the LiDAR sensor (Wehr 2009). The LiDAR sensors in most airborne systems perform ranging using a pulsed laser, as opposed to continuous wave lasers which are more common in terrestrial LiDAR sensors.

The target coordinates X_G are obtained in the registration, using the LiDAR equation (e.g., Habib et al. 2009):

$$X_G = X_0 + R_{yaw,pitch,roll} \cdot P_G + R_{yaw,pitch,roll} \cdot R_{\Delta\omega,\Delta\varphi,\Delta\kappa} \cdot R_{\alpha,\beta} \cdot \begin{bmatrix} 0 \\ 0 \\ -\rho \end{bmatrix} \tag{1}$$

where X_0 is the vector between the origins of the ground (Cartesian, e.g., WGS84 XYZ) and IMU coordinate systems, P_G is the offset between the LiDAR and the IMU coordinate systems, and ρ is the measured range. There are three rotation matrices that describe the orientation of the Cartesian coordinate systems with respect to each other: $R_{yaw,pitch,roll}$ relates the ground and IMU coordinate systems, $R_{\Delta\omega,\Delta\varphi,\Delta\kappa}$ relates the IMU and LiDAR coordinate systems, and $R_{\alpha,\beta}$ relates the LiDAR and laser beam (spherical) coordinate systems. Essentially, the measurement of the target position is done in a spherical coordinate system, and there is no redundancy in the actual measurement. The obtained target coordinates X_G can further be projected to a map coordinate system with orthometric heights, such as the terrestrial Gauss-Krüger KKJ-2 and N60 systems used in this thesis.

Geometric calibration is needed after installing a LiDAR system in order to determine the lever-arm components and bore-sighting angles (i.e., the mounting parameters; Habib et al. 2009). Random, systematic and trend-like geometric errors can exist in the LiDAR data. Random measurement errors are due to imprecise positioning, ranging and determination of sensor and mirror attitude, whereas systematic errors are mainly caused by fixed or time-dependent bias in mirror angles, ranging circuits, GNSS, and/or in the mounting parameters which are employed. The accuracy of point cloud coordinates also depends on the flying altitude and scan angles, as the influence of attitude parameters on the coordinates depend upon the range. The effect of random errors was simulated by Habib et al. (2009). The point errors in well-defined targets were 0.1–0.4 m in the horizontal, and 0.1–0.2 m in the vertical direction, when flying at an altitude of 1.2 to 2 km, and scanning at a 20° angle. Strip-adjustment is normally performed after a campaign to remove some of the bias in the mounting parameters (Toth 2009).

The scan pattern on the ground is obtained by deflecting the emitted pulses with a mirror mechanism. The aim is to generate as regular a point cloud as possible, i.e., to obtain an efficient spatial sampling. The spatial sampling can be controlled by flying speed, as well as by mirror frequency, mirror type, and mirror speed variations. Oscillating, polygonal, and Palmer scanning mirrors are the most commonly used in airborne systems. There is a trade-off between the mirror and receiver aperture sizes because increasing the receiver aperture requires larger mirrors, which consequentially require higher powers to operate, especially in regard to oscillating mirrors (Wehr 2009).

1.2.2 Measurement process

Overview

Pulsed LiDAR sensors send very short and highly collimated pulses of laser light. The reflected pulses are observed by a narrow-field-of-view receiver in hot-spot view-illumination geometry (Figure 1). In vegetation, the targets are mostly diffuse reflectors and only a tiny portion of the transmitted photons reach the receiver’s aperture and mirror. The mirror directs the incoming photons through filtering optics to a sensitive and fast light detector operated in either multi-photon or single-photon (photon-counting) mode (Stilla and Jutzi 2009). Conventional multiphoton DR and WF systems differ from each other only in their recording logic (analog echo-triggering and ranging vs. digitization and storage of the WF samples). The recorded observations are affected by characteristics of the transmitted pulse, the interaction of the photons with the target and atmosphere, and the characteristics of the signal path in the receiver.

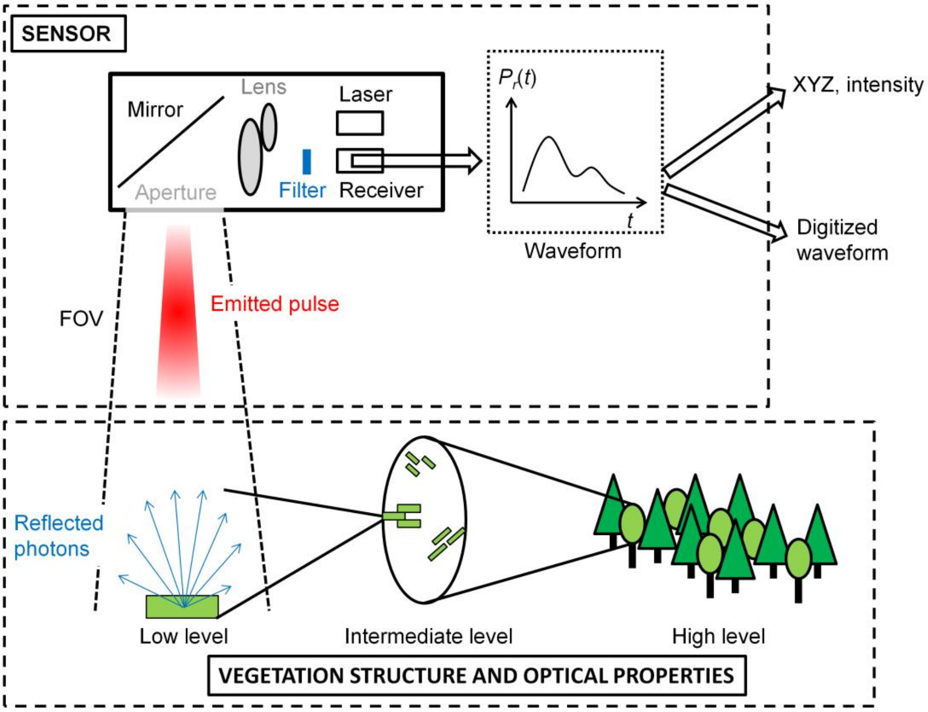

Figure 1. Illustration of a simplified LiDAR sensor and the factors affecting the measurements. The data recorded are influenced by the sensor parameters (emitted pulse, receiver characteristics), and the vegetation structure and optical properties at various levels. Low level: the optical properties (e.g., BRDF) of individual leaves or needles. Intermediate level: the arrangement of foliage on the branches and the branching structure within tree crowns. High level: the spatial arrangement of trees in forest stands.

Transmitted pulse

Laser light is generated by the stimulated emission of photons in the laser source. The laser source determines the wavelength (λ) of the emitted radiation. High-power pulsed diode lasers at 905 nm and diode-pumped solid state lasers at 1064 and 1550 nm are the most common sources used in airborne applications (Pfenningbauer and Ullrich 2011). Frequency-doubling can be used to achieve green laser (e.g., at 532 nm, Petrie and Toth 2009). The selection of λ affects the level of sunlight-induced noise and atmospheric transmission losses (Pfenningbauer and Ullrich 2011). The typical duration or width of the emitted pulse is 4–10 ns, when it is defined as full width at half maximum (FWHM) (Stilla and Jutzi 2009). Eye-safety regulations set the maximum permitted energy density (J m^{-2}), which depends on the λ, peak power, exposure time (FWHM), and footprint size. Footprint size defines the energy density through scan range and beam divergence. The applied λ affects eye-safety because the human eye is most sensitive to λ of 400–1400 nm. More powerful lasers can be used at 1550 nm (Wehr and Lohr 1999; Pfenningbauer and Ullrich 2011). The typical values of the peak power used in airborne sensors are between 1 and 30 kW (e.g., Petrie and Toth 2009; Chasmer et al. 2006). In addition to peak power, the beam divergence and within-footprint irradiance distribution characterize the emitted pulse. Typical values for the beam divergence in small-footprint systems are 0.15–1 mrad. The within-footprint irradiance distribution is often modeled as either a Gaussian or cylindrical distribution (top-hat form) (Jutzi and Stilla 2006a), although little is known about the actual distributions of commercial sensors.

Interaction of the pulse with vegetation

When encountering vegetation, photons are reflected, absorbed or transmitted and can undergo multiple interactions before being finally absorbed or escaping the volume. The reflected directional radiance (W sr^{-1} m^{-2}) in certain view-illumination geometry depends on the incident irradiance, the projection area of the scatterers and their optical properties and orientation, and the overall ‘structure’ (the relative orientation of scatterers) (Knyazikhin and Marshak 1991). The structure affects multiple scattering and mutual shading of the scatterers. Because of the hot-spot geometry, the first-order scattering in LiDAR is not affected by mutual shading (Kuusk 1991). For the same reason, the contribution of multiple scattering is often considered to be relatively low compared to passive optical data (Disney et al. 2006, Roncat et al. 2014b). However, this depends on vegetation characteristics, and multiply scattered photons can account for as much as 43% of the total energy reaching the receiver (study III). A particular trait of LiDAR is the coherence of the laser light. Thus, wave phenomena can affect the backscattered radiance (Wagner 2010). An example is the interference which causes speckle (Goodman 1976) and coherent backscatter (Hapke et al. 1996). The former is random in nature and averages out if the receiver’s instantaneous field-of-view (iFOV) is large enough (Wagner 2010), whereas the latter causes a stronger backscatter (different BRF) compared to incoherent light. Overall, the received signal represents the time-dependent sum of the energy of all of the reflected photons from within the receiver’s iFOV. The signal is extended in time due to the width of the emitted pulse, multiple scattering, and the volumetric media of illuminated scatterers. In addition to structure, the directional optical properties of the scatterers affect the backscattered radiance. In forest canopies, the foliage constitutes the majority of the projected area that is visible from above. The scattering characteristics of plant leaves in near-infrared (NIR) and shortwave-infrared (SWIR) regions are mainly driven by the internal leaf structure because the absorption by pigments is low (Walter-Shea and Norman 1991). In NIR, over 90% of the radiation is reflected or transmitted. The reflectance and transmittance in SWIR are lower compared to NIR because of the higher absorption by leaf water in SWIR. One of the available laser wavelengths (1.55 µm) is close to a major water absorption band at 1.43 µm. This explains why moisture on the leaf surface strongly affects the absorption at 1.55-µm wavelengths (Figure 2). Leaves differ from Lambertian (perfectly diffuse BRDF) reflectors, although Lambertian behavior is often assumed in radiative transfer models. Typical Leaf BRDFs have both diffuse and specular components, whereas the directional distribution of transmitted light (BTDF) is closer to Lambertian (Walter-Shea and Norman 1991). The BRDF and BTDF measurements of individual leaves are difficult to attain (Walter-Shea and Norman 1991; Bousquet et al. 2005), particularly in hot-spot geometry and using laser light (Kaasalainen et al. 2005).

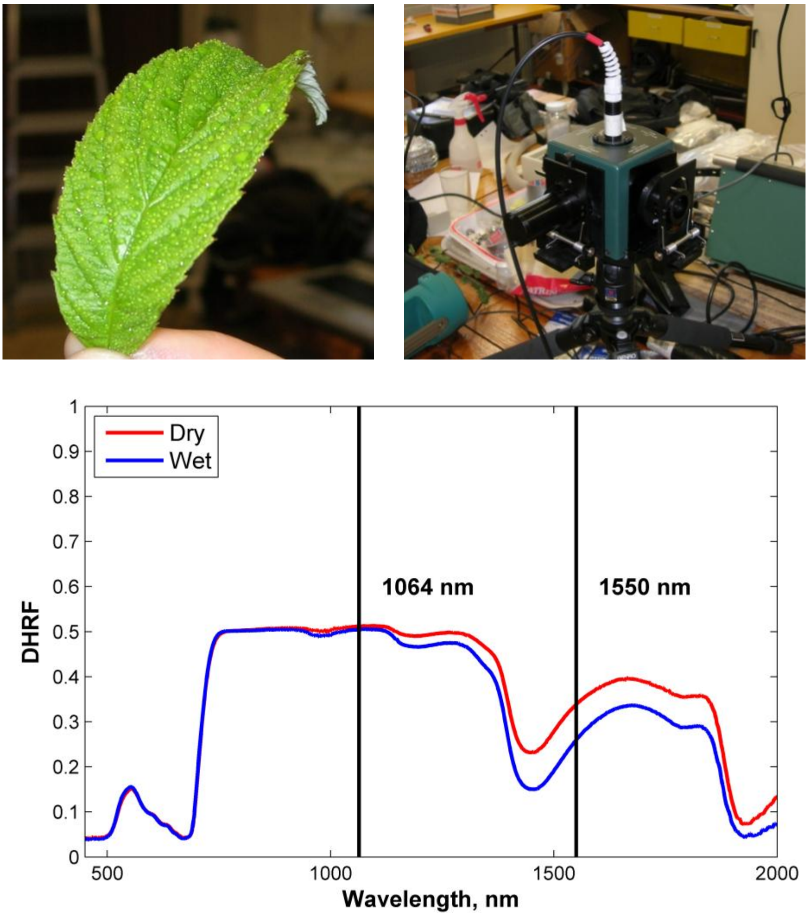

Figure 2. Directional-hemispherical reflectance spectrum of a raspberry leaf (bottom) that was measured dry or with droplets of water on the surface (top left). The vertical lines denote the two most common wavelengths in airborne LiDAR sensors. The measurements were performed with a spectroradiometer and an integrating sphere (top right).

Receiving and recording the signal

In the early days of ALS, maximizing the signal-to-noise ratio (SNR) was important because SNR affects the ranging accuracy (Wehr and Lohr 1999). If the aim is to quantitatively deduce the target characteristics from LiDAR data, the user must know the function that relates the instantaneous at-sensor signal with the actual observations recorded. WF recording has made the measurement process more transparent, but there are still many uncertainties, especially because the response functions of commercial sensors are not exactly known (Roncat et al. 2014b). The incoming signal is collected from within the receiver's iFOV through an aperture, and directed through collimating optics to a photosensitive detector. This converts it into an electronic signal to be further processed (Wehr 2009). The receiver's iFOV must be large enough to cover the footprint and to account for sensor movements during the travel time of the pulse, but also small enough to minimize the sunlight reflected by the variable scene and the medium. The receiver aperture determines the strength of the signal that reaches the detector by integrating an area of the instantaneous at-sensor irradiance field. The wide-band noise is reduced using a narrow band-pass filter in front of the detector (Wehr and Lohr 1999). The electronic signal must be amplified before the triggering of echoes or WF storage. Usually there is a trans-impedance amplifier that converts the photocurrent to voltage (Wehr 2009). Various noise components are introduced to the signal. In addition to the external solar noise, other possible noise sources include dark noise introduced by the detector, noise induced by the electronics (e.g., thermal noise), and quantization noise created in the A/D conversion (Baltsavias 1999a; Wehr and Lohr 1999; Ullrich and Pfenningbauer 2011). The sensor must operate at a wide dynamic range mainly because of range variation, and this causes signals to vary from 100- to 1000-fold when the range changes 10-fold and the transmitted power is fixed. A high dynamic range is achieved by adjusting the transmitted power or by applying different receiver sensitivity settings. Leica has manufactured sensors that have adjustable laser power (up to 20 dB) and automatic gain control (up to 3 dB) in a receiver that is run in high-gain mode (e.g., Korpela 2008; Vain et al. 2010). Many modern sensors employ several receivers of varying sensitivity (Jalobeanu and Gonçalves 2012). Each of the system components has bandwidth characteristics which may differ according to signal strength. The characteristics of all the components form the impulse response of the system (Jutzi and Stilla 2006b). In many DR sensors, the signal is recorded on-the-fly with analogue circuits that employ an echo detection algorithm (Wagner et al. 2004). The WF systems digitize the signal continuously and when there is a meaningful signal, the storage function is triggered. Ullrich and Pfenningbauer (2011) presented a classification of WF-recording LiDAR systems based on their recording logic. The sensors were classified as 'full-waveform' or 'echo waveform', depending on whether they digitized the WFs of both the emitted and received pulses, or only the received pulse. There are also sensors that deliver both DR echoes and WF data. Data from these sensors were classified as 'tightly-coupled echo signal samples' if the sensor recorded WF data and performed online WF processing, and 'loosely-coupled echo signal samples' if the sensor performed discrete ranging and WF recording in separate, yet synchronized circuits.

Airborne small-footprint sensors

Table 1 lists the airborne small-footprint sensors of three major manufacturers (Leica 2015; Optech 2015; Riegl 2015). Models that have a WF recording option are included. There are sensors for various purposes, which is reflected in the maximum possible operating altitude (Max. range) parameter. The maximum PRF has progressively increased until recently and some sensors operate at a PRF of above 500 kHz. The PRF is limited by the travel-time of the pulse and the measurement-cycle overhead of the receiver (Roth 2011). Many current systems are capable of handling multiple pulses in the air and some even split the emitted beam, thus doubling the effective PRF at the cost of 3 or more dBs (Roth 2011). Riegl sensors rely entirely on WF recording and the echo extraction is performed in the post processing phase. The other manufacturers have loosely-coupled systems that record both DR and WF data. Because of the high flow of data, the recording rate of WF pulses is restricted to 120 kHz (in Leica sensors) and 125 kHz (in Optech sensors). The utility of WF recording in improving the vertical resolution is gradually vanishing since some sensors already record an unlimited number of DR echoes. Currently, the only manufacturer providing a multispectral system in one sensor is Optech, with their 'Titan' model operating at 532, 1064 and 1550 nm.

Table 1. Examples of commercial airborne LiDAR sensors that can deliver WF data.

Model	Max. effective PRF, kHz	Max. range, m[a]	Wavelength, nm	Beam divergence, mrad
		Leica		
ALS60	200	6300	1064	0.22 (1/e^2)
ALS70	500[b]	1900/4400/6300[c]	1064	0.22 (1/e^2)
ALS80	500/1000[b, c]	1600/3500/5000[c]	N/A	N/A
		Optech		
Galaxy	550	4700	1064	0.25 (1/e)
Orion	300	4000	1064/1541[c]	0.25 (1/e)
Pegasus	500	5000	1064	0.25 (1/e)
Titan	900[d]	2000	532/1064/1550	0.35/0.7 (1/e)
		Riegl		
LMS-Q680i	266	1600	1550	≤0.5 (1/e^2)
LMS-Q780	266	4700	N/A	≤0.25 (1/e^2)
LMS-Q1560	532[b]	4700	N/A	≤0.25 (1/e^2)

[a] Depends on the target reflectance. The definitions differ.

[b] Two receivers with their iFOVs 'viewing' in different directions.

[c] Depends on the specific model version

[d] 300 kHz per band

1.2.3 Theoretical formulation and radiometric calibration of LiDAR observations

The time-dependent analogue signal that is directed to the sensor's DR circuit or WF digitizer, results from a convolution of the transmitted pulse with the target and receiver responses (Figure 3). The properties of the transmitted pulse and receiver response vary according to sensor specifications. The target response is affected by both the target itself and the sensor used (e.g., by wavelength or footprint size). In addition, there are other parameters that influence the WF in a linearly multiplicative manner, such as the scanning range, receiver aperture, or atmospheric attenuation.

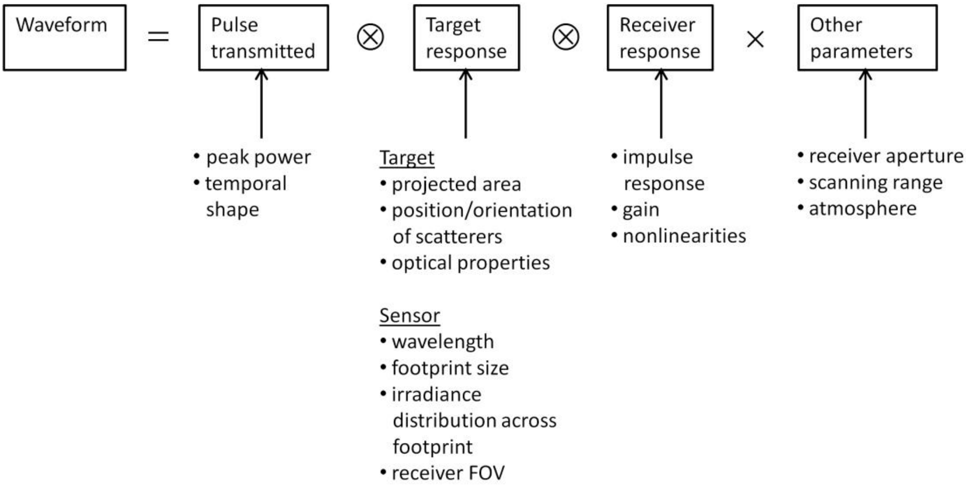

Figure 3. Conceptual model of the factors affecting the LiDAR waveform. The symbols ⊗ and × denote convolution and multiplication, respectively.

Rigorous mathematical formulation of the measurement process is needed for forward modeling, i.e. in explaining and understanding the measurement, and in the inversion of the measurements in order to derive physical target properties, which is called calibration (Roncat et al. 2014b). The most commonly used model for LiDAR measurement is the radar equation (Jelalian 1992). Its derivation for LiDAR data was presented in Wagner et al. (2006) as:

$$P_r(t) = \frac{D^2 \eta_{sys} \eta_{atm}}{4\pi\beta^2 R^4} \cdot P_t(t) \otimes \sigma(t) \otimes \Gamma(t) = \frac{D^2 \eta_{sys} \eta_{atm}}{4\pi\beta^2 R^4} \cdot S(t) \otimes \sigma(t) \tag{2}$$

where $P_r(t)$ is the amplitude of the signal received as a function of time, i.e., the analogue WF. It is either interpreted for range and intensity in DR sensors, or digitized at short time-intervals in WF-recording systems. D is the diameter of the circular receiver aperture, β beam divergence, R scanning range, $P_t(t)$ power transmitted, $\sigma(t)$ target differential backscatter cross-section, $\otimes$ convolution operator, $\Gamma(t)$ the receiver impulse response, and η_{sys} and η_{atm} represent the system and atmospheric losses, respectively. Because the convolution is commutative, $P_t(t)$ and $\Gamma(t)$ can be merged to form the system WF, $S(t)$. σ is composed of the target reflectivity (ρ), area (A), and the directionality of scattering (Ω):

$$\sigma = \frac{4\pi}{\Omega} \rho A \tag{3}$$

If the target is shaded by another target, σ is 'apparent' backscatter cross-section, meaning that it represents the areas illuminated by the laser beam. Equation 2 states that, in addition to the target characteristics (Equation 3), the instantaneous power entering the aperture is related to β, D, $P_t(t)$, R, and η_{atm}, while $\Gamma(t)$ and η_{sys} influence how this signal is finally stored as a WF. Radiometric normalization or calibration aims at removing some or all of these effects from the recorded intensity or amplitude data.

Corrections for the effects of R and η_{atm}, and varying receiver gain are referred to as normalization. Some sensors have look-up-tables to correct for non-linear response. The effects of R and η_{atm} are relatively straightforward to remove using empirical or theoretical correction models (e.g., Höfle and Pfeifer 2007). If the receiver's sensitivity (gain) varies during the acquisition, an extension of the model is needed (Korpela 2008; Vain et al. 2010). Well-defined (planar, area-extended) targets of homogeneous reflectance are needed for the estimation of the model parameters. Normalized data are comparable across one acquisition, during which the transmitter settings remain unchanged, but the normalized amplitude or intensity values are digital numbers without physical meaning. Additionally, the radar equation assumes that the amplitude values are in linear dependency with instantaneous power entering the aperture. If this is not true, the range normalization remains inaccurate.

Solving the necessary parameters in order to derive physical target parameters is referred to as calibration. This can be performed as vicarious calibration, i.e., using field calibration targets with known hot-spot BRF (Kaasalainen et al. 2009). In vicarious calibration, the σ is calculated for the calibration targets, and the system WF and other sensor parameters are then solved using Equation 2 (Wagner 2010). If amplitude values are linearly related to the power received, and the zero point (offset) is known, one target is sufficient for calibration. Otherwise, several targets of varying BRF are needed. Absolute laboratory sensor calibration would be an alternative to vicarious calibration. For an absolutely calibrated sensor, the power of the emitted pulse and the receiver response to instantaneous at-sensor radiance are known from calibration. Thus, the digital amplitude values can be directly converted to power entering the receiver, and the σ can be solved from Equation 2, using the emitted pulse power, the power entering the receiver, and the additional atmospheric parameters. Currently, absolute calibration of WF sensors does not exist, unlike digital airborne cameras (Beisl 2006). If the temporal shape of σ (i.e., $\sigma(t)$) is required instead of its integral, a solution for de-convolution is needed in both vicarious and absolute calibration procedures. The most common approach is to fit Gaussian functions into the transmitted and received WFs, thus enabling de-convolution to be solved analytically (Wagner 2010).

Finally, it should be noted that there are factors that may make the calibration process ill-posed in the context of vegetation. First, vegetation comprises of scatterers that are neither point-like, nor area-extended, implying that the σ possibly depends on the footprint diameter, but may not be directly proportional to footprint area (cf. calibration to backscatter coefficient in Wagner 2010). For example, it has been shown that range normalization is ambiguous in forest canopies (Korpela et al. 2010a; Gatziolis 2011). Second, the backscattering in targets smaller than the footprint depends on the distance of the target from the footprint center, because the degree of irradiance decreases away from the footprint center.

1.2.4 Interpretation and use of waveform LiDAR data

Since the first WF sensors emerged in the mid-2000s, the processing and use of WF data has gained much attention in literature. However, the methods associated with WF data are still not as mature as those associated with DR data. Mallet and Bretar (2009) and Hollaus et al. (2014) provide good reviews of WF processing methods. The benefits of WF data can be summarized as follows: First, the range measurements (search of reflectors) can be performed in post processing with user-defined algorithms. In general, WF data can provide more echoes compared to DR systems (Reitberger et al. 2008; Chauve et al. 2009), although the characteristics of the emitted pulse (e.g., footprint and pulse width) and the geometry of the target influence the number of digitized echoes. Second, additional echo parameters (width, amplitude) can be derived and used in classification tasks (e.g., Wagner et al. 2008; Reitberger et al. 2008; Heinzel and Koch 2011; Mallet et al. 2011). Third, with de-convolution it is possible to derive the target backscatter cross-section that is not blurred by the emitted pulse width and receiver response (Wu et al. 2011). The de-convolution is linked with the radiometric calibration presented in Section 1.2.3 (Wagner 2010). The most common way to process WF data is to fit Gaussian (Hofton et al. 2000; Wagner et al. 2006) or some other functions (Mallet et al. 2010; Roncat et al. 2014a) to the WFs. It then becomes possible to calculate the locations (peaks) and additional attributes for each echo. Direct calculation of attributes from the raw WF is also possible (Harding and Carabajal 2005; Yu et al. 2014). De-convolution can be performed either using the fitted functions (Wagner et al. 2006; Roncat et al. 2011) or entirely in the digital domain (Jutzi and Stilla 2006a; Wu et al. 2011). In the latter case, the problem of interpreting the de-convolved WFs remains, but it is possible, for example, to again fit Gaussians or some other functions to them to aid in the process.

1.3 Analyses of airborne LiDAR data in forest vegetation

1.3.1 Interpretation approaches and information sources

The fundamental task in RS of vegetation is to establish the relation between the RS features (metrics) and the vegetation variables of interest (Figure 4). This relation can be based on empirical or physical models. Most of the LiDAR applications in forestry are data-driven with empirical models to link plot or stand-level forest variables with the LiDAR point cloud features (Næsset 2002; Packalén and Maltamo 2007). This is commonly referred to as the area-based approach. Individual tree RS (Nyyssönen 1955; Talts 1977) that can be also applied to LiDAR data (Hyyppä and Inkinen 1999; Persson et al. 2002) bears closer resemblance to a physically-based interpretation, because tree height and crown dimensions are measured directly. Empirical models or non-parametric estimation methods are also needed in these approaches for species identification and the allometric estimation of stem dimensions (Vauhkonen et al. 2010; Yu et al. 2011). The division is not strict and there are solutions available that operate at the level of tree groups (Breidenbach et al. 2010). The benefits and challenges associated with the various approaches have been reviewed by e.g., Hyyppä et al. (2008) and Vauhkonen et al. (2014a).

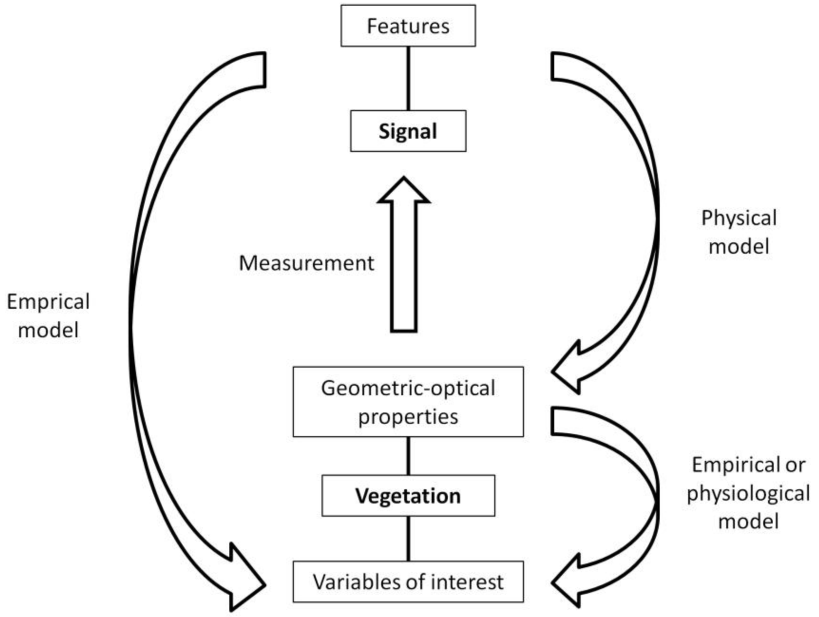

Figure 4. Interpretation of vegetation properties from optical RS data.

1.3.2 Influence of vegetation properties on backscattering

LiDAR data provide both geometric and radiometric information that is used to calculate features. In essence, geometry and radiometry are intertwined and one does not exist without the other. To exemplify: sufficient backscattering is required for ranging, but weak backscattering is 'left unnoticed', widened backscattering implies geometric ambiguity and any backscattering results simultaneously from the target geometry and reflectivity that exist in a volume of vegetation. Geometry, as I define it, has mainly to do with the accuracy of the pulse path and the determination of scatterer coordinates. Radiometry meanwhile is linked with the properties of the time-dependent observations of the returning photon surge. Each LiDAR echo has geometric attributes (XYZ, height), and potentially, intensity recording or additional attributes may be extracted from WF data. I use term ‘echo attributes’ to denote any such attributes (e.g. XYZ, height, DR intensity, WF attribute). Additionally, I refer to ‘DR intensity’ and ‘WF attributes’ to mean the DR intensity recordings or echo attributes extracted specifically from the WF. Features are computed from the attributes as spatial distribution metrics, as LiDAR measurements are spatial by nature. This systematic is of course arbitrary. For example, features can be computed directly from the WF using the spatiality of the WF energy, without linking it explicitly to echoes.

The LiDAR signal is driven by the geometric-optical properties of vegetation on various scales (Figure 1). The majority of studies that have linked airborne LiDAR measurements with vegetation characteristics have been empirical and indirect, in the sense that the linkage was established with relatively easily measurable vegetation variables such as height, stem volume, or canopy cover extracted from digital hemispherical photographs. The early studies demonstrated the relations between the height distributions of LiDAR echoes and tree heights (Nilsson 1996; Næsset 1997a), and the vertical distribution of leaf area (Magnussen and Boudewyn 1998), although in the latter study leaf area was predicted based on stem volume. These relations resulted in the development of the area-based height distribution metrics that are used in operational inventories to predict the growing stock (e.g., Næsset 2002; Packalén and Maltamo 2007). The percentage of ground echoes is related to canopy gap fraction, which can be used to estimate LAI (Solberg et al. 2009; Korhonen et al. 2011). The DR intensity and WF attributes are more difficult to interpret. In theory they are related to the size, position, orientation and optical properties of the scatterers along the pulse path (Wagner et al. 2006). There is some empirical evidence for this (e.g. Hollaus et al. 2009; Korpela et al. 2010b), although these studies were performed at the level of individual tree crowns. There appear to be very few studies that explicitly link pulse-level measurement data with vegetation characteristics (Doneus et al. 2010). This is a difficult task because detailed field reference data are needed, and the co-registration of the LiDAR and field reference data must be very accurate. Also many of the plot- or tree-level studies suffer from a lack of accurate field reference measurements for the vegetation structure. Simulation studies form an alternative to empirical approaches and have been used to model both large footprint (Sun and Ranson 2000; Ni-Meister et al. 2001; Kotchenova et al. 2003), and small footprint (Holmgren et al. 2003; Morsdorf et al. 2009; Disney et al. 2010) LiDAR measurements. Simulation models should be correctly parameterized to provide comparable results to those in real settings of complex and variable vegetation.

The response of LiDAR data to different tree species has been a subject of great interest to researchers. Species identification is important from a forest management point of view, but also because the canopy geometry, leaf angle distribution, leaf mass and area, and their allometric dependencies are species-specific and linked with important forestry variables (such as stem volume and growth). As a consequence, a mixture of tree species shows as differences in LiDAR height and density metrics (Næsset and Gobakken 2008). A recent review of studies dealing with species identification in LiDAR and passive data was conducted by Vauhkonen et al. (2014b). Generally, different distribution metrics of DR intensity and WF attributes have proven useful for the purposes of species classification of individual trees (Holmgren and Persson 2004; Ørka et al. 2009; Korpela et al. 2010b; Reitberger et al. 2008; Hollaus et al. 2009; Heinzel and Koch 2011). The distribution metrics that are computed from tens of pulses per tree exhibit species-specific patterns, which are revealed by statistical reasoning. It seems that pulse-level signals characterize the small-scale variation in density, position, orientation and optical properties of foliage, which are (to a highly varying degree) characteristic to species. Relatively little attention has been paid to quantifying the sources of variation at species level in comparison to other factors that affect the geometric-optical properties. These factors include, for example, tree height (Ørka et al. 2009; Korpela et al. 2010b), or site type (Korpela et al. 2010b).

1.3.3 The role of acquisition and sensor characteristics

A reduction of pulse density lowers the sampling intensity. Thus, the abrupt changes in canopy geometry are blurred and canopy heights become underestimated (Gobakken and Næsset 2008; Disney et al. 2010). In addition, the uncertainty of distribution metrics due to random variation remains higher (Gobakken and Næsset 2008). This holds true to any LiDAR metric that is subject to random (non-correlated) between-pulse variation within the estimation unit – for example a tree crown or a rectangular area.

Acquisition height, footprint size, and PRF in DR data have been reported to exercise an effect on height and density metrics, as well as on the proportions of echo categories, which include first, single, last etc. (Hopkinson 2007; Næsset 2009). With other parameters being constant, an increase of the scan range or footprint size reduces the at-target irradiance, and thus the SNR for linear and blob-like targets (smaller than the footprint). The total target area that is illuminated increases, as does the number of distinct canopy objects which are intersected by the pulse. The scan range also affects the SNR through spherical loss as the aperture corresponds to a smaller solid angle, as well as through atmospheric transmission losses. A high PRF may only be achievable by reducing the peak power of the pulse, which reduces the SNR. The effects are often intertwined, e.g. an increase of flying altitude increases the footprint size. Also, the effects of footprint may be confused with the effects of pulse density (Hopkinson 2007), but there can be opposite effects as well. For example, an increase of the footprint size at fixed output power can reduce the number of multi-echo pulses, because of a reduced SNR for objects smaller than the footprint. On the other hand, the number of objects along the pulse path may increase, thus potentially increasing the number of echoes, and the pulses that reach the forest floor therefore have less energy and exhibit less illumination variation compared to narrow pulses. Similar comprehensive tests as those reported for DR data (Hopkinson 2007; Næsset 2009) have not been performed for WF data. Although the underlying principles are the same, in WF data the range detection method (see Wagner et al. 2004) does not affect the interpretation of the test results. Also, the number of possible dependent (e.g., the WF attributes such as echo width and energy) and independent (e.g., pulse width, sampling frequency) parameters is larger in WF data. Disney et al. (2010) studied the sensor effects on canopy heights estimated from LiDAR data through simulation, and the range detection method and footprint size were seen to affect the measurements of canopy height. Increasing the footprint size led to an increase in the measured canopy heights because the probability of a sufficient portion of the footprint hitting a treetop was higher. In the experiment, the emitted power was controlled; i.e. the average at-target irradiance was constant.

Increasing the scan zenith angle increases the path length and may also affect levels of pulse penetration in certain canopy geometries. There may also be changes in the proportion of ground echoes and in the height distribution of canopy echoes. Analyses of simulated and empirical data suggest that these effects are insignificant from an operational viewpoint - at least with small (<10–15°) scan zenith angles (Holmgren et al. 2003; Disney et al. 2010; Ahokas et al. 2011). The term scan zenith angle is used here to distinguish the instrument scan angle which is not affected by the attitude of the platform, and to draw a parallel with the terminology used when describing passive optical RS. The scan zenith angle is used to calculate the incidence angle. In turn, this affects the backscattered radiation in Lambertian planar surfaces (Wagner 2010), because the probability of a photon scattering in a given direction is inversely proportional to the cosine of the angle between that direction and surface normal (Smolander and Stenberg 2003). Canopies are volumetric and comprise a distribution of scatterer surface geometries, yet the effects of scan zenith angle on the echo attributes in vegetation contexts are poorly understood.

1.4 Rationales

Pulsed small-footprint LiDAR sensors perform efficient and accurate 3D probing of vegetation, and have therefore gained a strong foothold in the remote sensing of forests. LiDAR measurements show a response to vegetation and sensor characteristics, and there is an urgent need for a more thorough physical understanding of these interactions. Physical understanding would be particularly advantageous in determining new data interpretation techniques, in reducing the need for field training data, and in optimizing sensors for vegetation applications. The advent of WF-recording sensors in recent years promotes a development towards physically-based interpretation, because the measurement process is more transparent when compared to DR sensors, and WF data contains more information about the intersected vegetation.

1.5 Objectives

The main overall objective of the thesis was to improve the understanding of LiDAR measurements of forest vegetation. The secondary objective was to derive more meaningful information from WF LiDAR data. The specific objectives are listed below:

1. To interpret DR LiDAR measurements for explaining the characteristics of understory trees, and to study how the geometry and radiometry of the measurements are affected by transmission losses in the upper canopy layers (Study I).

2. To develop a specific method of close-range photogrammetry, and to use it to examine LiDAR backscattering and WF attributes at the scale of individual pulses (Study II).

3. To develop a WF LiDAR simulation model, to validate it against real data, and to test the sensitivity of simulation results to variations in vegetation parameters (Study III).

4. To describe how vegetation, sensor, and acquisition characteristics affect WF attributes at individual pulse, vegetation sample, and individual tree levels (Studies III and IV).

5. To test WF data for the purposes of classifying low vegetation in young stands, and tree species in more mature forests (Studies III and IV).

2 MATERIALS AND METHODS

2.1 Study area

All of the experiments were conducted in Hyytiälä, Southern Finland (61°50′N, 24°20′E). The forests in the area are of a boreal coniferous type. Most of the stands are commercially managed and even-aged. Scots pine (*Pinus sylvestris* L.) and Norway spruce (*Picea abies* (L.) Karst.) form the majority of the growing stock, but there is a varying degree of deciduous mixture (mainly birches, *Betula pendula* Roth and *Betula pubescens* Ehrh.) in many of the stands (Korpela 2006). RS research with passive optical and LiDAR data has been actively conducted in the area over the past 15 years, and research activities have been concentrated on a relatively small area of 2×6 km. A large number of LiDAR campaigns with varying sensor- and acquisition parameters were available stemming from 2004, and more were acquired during the course of the thesis work. In addition, a time series of accurately oriented high-resolution aerial images from 1946 to 2013 was available for experiment (Korpela 2006). The nearby SMEAR II station is able to provide weather and atmospheric optical thickness observations (Junninen et al. 2009). Permanent fixed-area forest plots of varying size (N = 178) formed the basis of the field experiment, and additional field measurements were conducted for some of the studies of this thesis (Section 2.2).

2.2 Field reference data and positioning methods

Studies I, II, and IV utilized the permanent sample plots described earlier. Individual tree measurements in the plots were used in study IV. Measurements of understory trees were performed in two of the plots for study I, and close-range field photogrammetric imagery was acquired in three of the plots for study II. Measurements in seedling and sapling stands were performed for study III.

The permanent sample plots were established between 1995 and 2011. The key idea has been to position the trees as accurately as possible to enable the linking of individual trees to RS data. A total station (tacheometer) was used prior to 2006, and a photogrammetric method later. In the photogrammetric method, the user performs manual photogrammetric measurements of the tree tops of larger trees (image ray intersection or LiDAR monoplotting principle, see Figure 6). The tree tops then comprise control points in field triangulation that follows (Korpela et al. 2007). Network GNSS with a 4-m-high antenna was used in one young stand. The measurements comprised basic forest inventory variables such as diameter at breast height, tree species, and status (living, dead, shape, symmetry, vigor of the crown). Tree height and crown base height were measured for sample trees. The minimum diameter of the trees included varied between 36–86 mm. The plotwise threshold was always set to include all trees higher than 40% of the dominant height. A summary of the field plots is provided in Table 2. The total number of standing trees in the experiment was 25427 in the autumn of 2014. Photo-visible pine, spruce and birch trees (N = 9930) in a subset of plots re-visited in the summer of 2013 were used in study IV.

Table 2. Characteristics of the field plots in the study area.

Stand variable	Mean	SD	Min	Max
Age, yr.	62	27	22	142
Stem number, N ha^{-1}	995	524	75	2861
Diameter at breast height, cm	22.7	5.9	10.5	43.7
Height, m	19.9	4.2	6.6	31.1
Height growth, m yr^{-1}	0.27	0.10	0.01	0.59
Basal area, m^2 ha^{-1}	26.1	7.2	2.4	47.2
Stem volume, m^3 ha^{-1}	253	98	16	607
Pine, %	43	36	0	100
Spruce, %	43	34	0	100
Birch, %	12	20	0	100
Other, %	1	8	0	87

An intensive field measurement campaign to map understory trees was performed for study I. The measurements were conducted in two permanent sample plots in the summer of 2009. The plots were selected to represent a middle-aged and a mature pine forest with intra-plot density variation in the understory (Figure 5). The study was confined to one-species stands because of tedious measurements, and because the transmission loss modeling in the LiDAR data required stationary reflectance characteristics in the upper canopy layer. All trees higher than 30 cm were positioned and measured. A specific mapping method was developed, because it was not possible to achieve sub-decimeter-level georeferencing accuracy using GNSS in a dense forest. The mapping was performed by adjusting a cable between two large trees, and by measuring distances along and perpendicular to the cable. The cable end-points were positioned by triangulation and trilateration, with azimuth and distance observations to photogrammetrically positioned large trees which served the purpose of control points. The internal XY accuracy of the understory tree map was 0.07 m, based on field control measurements. The offsets between the tree map and LiDAR data were estimated to be 0.20 m at maximum (see also Section 2.3.2). The height and species of all individual trees (N = 5496) was recorded.

Figure 5. The sample plots in which intensive measurements of understory trees were performed. Left: 52-year old pine stand (medium to high fertility). Right: Mature pine stand (low to medium fertility).

An experiment involving close-range field photogrammetry formed the basis of study II. The idea was to take a network of vertical and oblique images of the canopy from below, and to solve the camera exterior orientation (EO) parameters so that individual LiDAR pulses could be back-projected onto the images. The images were taken with consumer-grade digital cameras that were calibrated and solved for interior orientation (IO) parameters: camera constant, principal point of best symmetry, and lens distortions. The camera was always attached to a leveled monopod of known dimensions. The camera azimuth and tilt were approximately known, so that the camera rotation and projection centers could be calculated for an accurate initial approximation, in a subset of cases in which the camera location was marked and measured with a total station. The workflow was as follows:

- Establishing a local coordinate system and a network of known camera locations and canopy tie/control points, using a total station with a prism for either direct positioning or as a theodolite for the triangulation of objects in the air.

- Bringing the local coordinate system into the coordinate system of the LiDAR, using triangulation (azimuth observations) to known control points (trees or man-made structures) positioned in aerial images and LiDAR data.

- Image acquisition from (approximately) known and unknown camera locations. Upward-looking and oblique images were taken to strengthen the image block geometry.

- Tie point measurements. Triangulation of the images using weighted least-square bundle block adjustment, in which different weights were given to image observations of tie points and control points, coordinates of the control points and camera locations. The solution gave camera EO parameters in the coordinate system of the LiDAR.

A mature pine stand was imaged in the summer of 2011, and two 60yr old pine and spruce stands were imaged in the summer of 2012. In addition, leaf-off imagery of non-forest trees was performed in the vicinity of Hyytiälä forest station in the spring of 2012. The arrangement of image and tie points and the block geometry varied slightly between sites. The work resulted in 639 images (Table 3) that were analyzed in order to link canopy characteristics with the properties of individual LiDAR pulses.

Samples of trees and low vegetation in seedling and sapling stands were collected for study III. The measurements were performed in 2010 and 2012, within three weeks of the LiDAR campaigns to ensure that the vegetation was unchanged. The aim was to collect point samples (i.e., individual trees or circular samples of low vegetation) of typical species. The samples were collected semi-subjectively from the chosen stands in order to achieve a representative number of samples per species. In particular, we aimed at collecting samples of the three species for which geometric-optical models were then constructed. These were birch (*Betula pendula* Roth), raspberry (*Rubus idaeus* L.), and fireweed (*Chamerion angustifolium* (L.) Holub.). The samples were positioned using network GNSS. The height and species of each sample were recorded. In addition to point samples, fixed-area plots were measured in 2010. All woody species in the plots were positioned and measured for species and height. In 2012, subjective estimates of canopy closure (0–100%) were made for a subset of samples to approximate the effect of foliage density (LAI) on the LiDAR signal.

To quantify the effect of the LAI of low vegetation on the LiDAR features more precisely, an additional LAI field measurement campaign was undertaken in 2013 in raspberry canopies. The analyses carried out on these data are only reported in this Summary. Firstly, destructive measurements were performed in 21 1×1 m sample plots. The LAI was predicted based on the dry weight and specific leaf area (m^2 kg^{-1}) of the leaves. Regression models were fitted between total biomass and LAI. Secondly, 29 plots were measured and LAI was predicted based on the total fresh biomass. In total there were 50 plots. The LiDAR data for each plot were extracted from within a circle of homogenous vegetation around the original 1×1 m plot. The radius was determined in the field as 0.5 to 1 m.

Table 3. The sites of photography, cameras used and the number of images taken.

Stand	Basal area, m^2 ha^{-1}	Height, m	Camera	Number of images
140-yr old pine stand	30	26	Canon Powershot G6	301
60-y-old pine stand	24	17	Nikon D300	143
60-yr-old spruce stand	32	21	Nikon D300	143
Non-forest trees	-	-	G6 and D300	52

2.3 LiDAR data

2.3.1 Datasets and sensors

Nine LiDAR campaigns conducted between 2006 and 2013 were used in studies I–IV. Some of the campaigns included repetitions from different altitudes or with alternate sensor settings (Table 4), which therefore provided separate datasets. In total, there were 19 datasets. The sensors used were Optech ALTM3100 (Optech Inc., Toronto, Canada), Leica ALS50-II/ALS60 (Leica Geosystems AG, Heerbrugg, Switzerland), and Riegl LMS-Q680i (Riegl GmbH, Horn, Austria). The data were acquired from fixed-wing aircraft, except for the LMS-Q680i campaign where the sensor was mounted on a helicopter skid. The flying altitude and maximum instrument scan angle varied between datasets (Table 4). Swath width was from 270 to 2400 m, and the strip overlaps were from 20 to 85%. The Optech and Leica sensors had oscillating mirrors (sinusoidal scan pattern), and the Riegl LMS-Q680i had a rotating polygonal mirror that results in a regular point pattern.

Data from DR sensors (ALM3100, ALS50-II) were acquired prior to 2010. The sensors recorded up to four echoes per pulse emitted. WF data were available in all campaigns conducted since 2010. The digitization was at 1 ns sampling rate, except for two trials with the ALS60 set at a 2 ns sampling rate (Table 4). The receivers of the ALS60 and LMS-Q680i differ fundamentally in their functioning. The ALS60 records DR echoes and WF digitization is performed by an optional WDM65 module. The WF digitization is triggered by the detection of the first DR echo and the DR circuits employ thresholding to assure that noise is not measured. A continuous '38-meter-long' WF sequence of 256 (1 ns) or 128 (2 ns) samples with a bit-depth of 8 is recorded. The emitted pulse is not recorded. The LMS-Q680i digitizes both the emitted and returning pulse. The WF recording is restricted to meaningful sequences. Discrete echoes are found in WF analysis using Gaussian decomposition. The lengths of continuous amplitude sequences in LMS-Q680i are multiples of 80 and there can be several such sequences per pulse emitted. The wavelength (λ) was 1064 nm, except in the LMS-Q680i which operates at 1550 nm. The beam divergence was 0.3 mrad (measured at $1/e$) in Optech, 0.22 mrad ($1/e^2$) in Leica, and 0.5 mrad ($1/e^2$) in Riegl. Because of the differences in beam divergence and flying altitudes, the footprint size on the ground varied between datasets (Table 4).

2.3.2 Geometry and radiometry of the LiDAR measurements

A high level of geometric accuracy was essential, especially in studies I and II that examined pulse-scale phenomena. Calibration acquisitions were carried out on the way to Hyytiälä in urban areas to determine the mounting parameters (Equation 1). Strip adjustment utilizing strip-wise overlapping terrain models as 'tie data' was performed by the data provider to remove systematic and time-dependent errors. The geometric quality of the data was estimated using height control points measured with network GNSS, and by the visual examination of pulses in man-made and natural objects seen in aerial and close-range images (Figure 6). Additional ‘strip adjustments’ were carried out in studies I and II to improve the planimetric match between the field and LiDAR data. Understory trees were used as 3D control surfaces in study I, and branch silhouettes measured in upward-looking terrestrial images were used in study II (see also Section 3.2). The optimization criteria for estimating the XY offsets were the echo-stem distances of the highest LiDAR echo per 'control tree' and the proportion of incorrectly assigned echoes (study I), or the correlation between branch silhouette area and maximum amplitude value of the LiDAR pulse reflecting from the branch (study II). Between-strip discrepancies were not accounted for in study I, whereas the XY geometry of each individual strip in relation to the field data was optimized in study II. The XY discrepancies between field and LiDAR data were found to be less than 0.3 m.

Figure 6. A 26.7m Siberian fir (Abies sibirica L.) viewed using aerial and terrestrial images. The LiDAR data had four strips depicted by the colors on the terrestrial image, which provides a view direction that is parallel to the scan lines. The yellow and dark blue echoes are made by oblique pulses. The figure illustrates the research infrastructure and the general usefulness of terrestrial and aerial images for data visualization and quality control. Man-made and other clearly defined objects were used in a similar manner to assess the geometric quality of the LiDAR data. The figures illustrate the monoplotting principle used for the positioning of dominant/co-dominant trees in the permanent sample plots. The user manually points the treetop (white circle) in the aerial image, and the first LiDAR echo inside an 'epipolar cylinder' is projected onto the ray to solve the XYZ of the treetop.

Images courtesy of Ilkka Korpela.

Table 4. Summary of the most important parameters of the LiDAR datasets.

Year, date, time	Sensor	Altitude (AGL), m	Pulses m^{-2}	Max. instrument scan half-angle, °	WF recorded (sampling rate, ns)	Footprint diameter on ground ($1/e^2$), m	FWHM of system WF, ns[b]	Used in studies
2006, July 25, 16–17	ALTM3100	800	7.1	14	No	0.25[a]	-	I
2007, July 4, 16–17	ALS50-II	800	9.5	15	No	0.17	-	I
2008, Aug 23, 7–8	ALS50-II	900	3.2	32.5	No	0.22	-	I
2008, Aug 23, 7–8	ALS50-II	1900	1.9	32.5	No	0.45	-	I
2010, Jul 19, 15–18	ALS60	1200	4.9	15	Yes (1)	0.26	7.2	II, III, IV
2010, Jul 19, 15–18	ALS60	1900	2.8	15	Yes (1)	0.43	7.2	II, III
2010, Jul 19, 15–18	ALS60	3000	1.0	15	Yes (1)	0.66	10.1	II, III
2010, Jul 19, 15–18	ALS60	1900	3.0	15	Yes (2)	0.43	7.4	II, III
2010, Jul 19, 15–18	ALS60	3000	1.0	15	Yes (2)	0.66	10.2	II, III
2011, Aug 2, 19–22	ALS60	800	10.7	15	Yes (1)	0.17	7.8	II, IV
2011, Aug 2, 19–22	ALS60	1900	2.4	15	Yes (1)	0.44	7.8	II
2011, Nov 15, 7–11	LMS-Q680i	800	19.0	30	Yes (1)	0.39	4.3	II
2012, Jul 5, 19–22	ALS60	500	5.3	15	Yes (1)	0.11	7.8	II, III
2012, Jul 5, 19–22	ALS60	1000	5.4	15	Yes (1)	0.22	10.1	II, III, IV
2012, Jul 5, 19–22	ALS60	2000	3.2	15	Yes (1)	0.45	10.3	II, III
2012, Jul 5, 19–22	ALS60	2700	2.2	15	Yes (1)	0.61	10.4	II, III
2013, Jun 15, 21–00[c]	ALS60	700	10.1	15	Yes (1)	0.15	7.8	IV, Summary

[a] $1/e$

[b] Estimated using pulses from planar surfaces

[c] Includes strips acquired at 700, 800 and 900 m. Receiver AGC off. Output power fixed.

The DR intensity and WF amplitude values were affected by the scanning range (*R*). In addition, the sensors had different solutions for handling the large variations in the received power. Leica sensors were used by preselecting the output power in 1% intervals to account for the flying height, eye-safety, and the desired SNRs for average scene reflectivities of linear and well-defined surfaces. The remaining signal variation is subject to an automatic gain control (AGC) circuit that changes the receiver gain up to about 3 dB during the acquisition. Normalization formulae were used for correcting the *R* and AGC effects as:

$$I_{cal} = I_{obs} \times \left(\frac{R}{R_{ref}} \right)^{a} \times f(AGC) \tag{4}$$

$$I_{cal} = I_{obs} \times \left(\frac{R}{R_{ref}} \right)^{a} \tag{5}$$

In equations 4 and 5, I_{cal} and I_{obs} are the normalized and observed intensity/amplitude values, R is the scanning range, R_{ref} the reference range, and $f(AGC)$ the function that relates the receiver gain with an AGC voltage value stored for each pulse. The range correction power (a) and the formulations for the $f(AGC)$ differed in the individual studies. Equation 4 was used for Leica data, and Equation 5 was used for Optech and Riegl data.

The amplitude scale in the Riegl LMS-Q680i is non-linear with respect to power entering the receiver at the high-end, but due to the relatively high 800 m altitude and the high PRF, the observations were always in the linear range. The receiver of the ALTM3100 is in all probability very linear, as has been suggested in the analyses of Korpela et al. (2010a) and Gatziolis (2011). However, analyses of data acquired from multiple flying heights and AGC turned off revealed that the amplitude scale in the ALS60 sensor applied in 2011–2013 is in fact slightly non-linear with respect to the power entering the receiver at both high and low signal levels. This is probably due to the non-linear behavior of the transimpedance or AGC amplifiers (Ron Roth, Leica Geosystems - personal communication).

There were fundamental differences in the radiometry of the LiDAR measurements caused by λ, different system WFs, and the algorithms applied by the DR recording circuits in the Optech ALTM3100 and Leica ALS50-II. The dependencies on λ are illustrated in Figure 7, which demonstrates the outcome of the large differences of vegetation reflectance between 1064 and 1550 nm. The shape of the system WF and the functioning of the DR circuit could be analyzed in more detail in the datasets with WF recordings (Figure 8 and explanations therein). The varying FWHM of the system WF influenced range resolution, i.e. the separability of targets. Due to the constant fraction discriminator (CFD) algorithm in Leica sensors, the DR echoes from vegetation were often detected 1–2 ns (some decimeters in range) prior to the main peak of the WF (Figure 8). The exact functioning of the echo detection in the Optech receiver remains unknown.

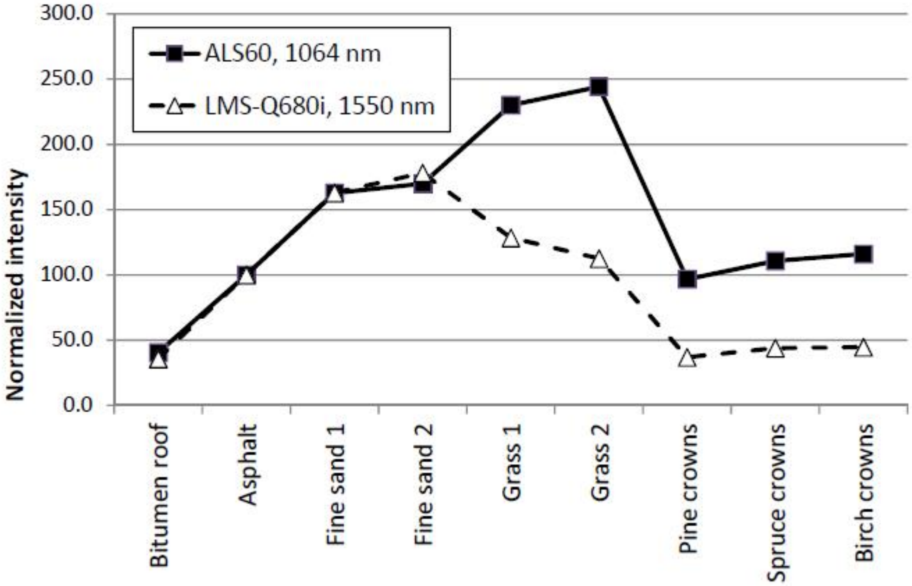

Figure 7. Averaged and normalized peak amplitude values (asphalt = 100) from planar surfaces of varying reflectance, as well as tree crowns. The figure demonstrates the effect of major differences in vegetation reflectance between 1064 nm and 1550 nm. The peak amplitude values for planar surfaces are linearly related to reflectance, whereas the differences in tree crowns are also due to footprint size and the species-specific structure. The acquisition heights were 2000 m for the ALS60 and 800 m for the LMS-Q680i. Due to differing beam divergence (0.22 vs. 0.5 mrad), the footprint sizes were almost equal 0.44 m and 0.40 m.

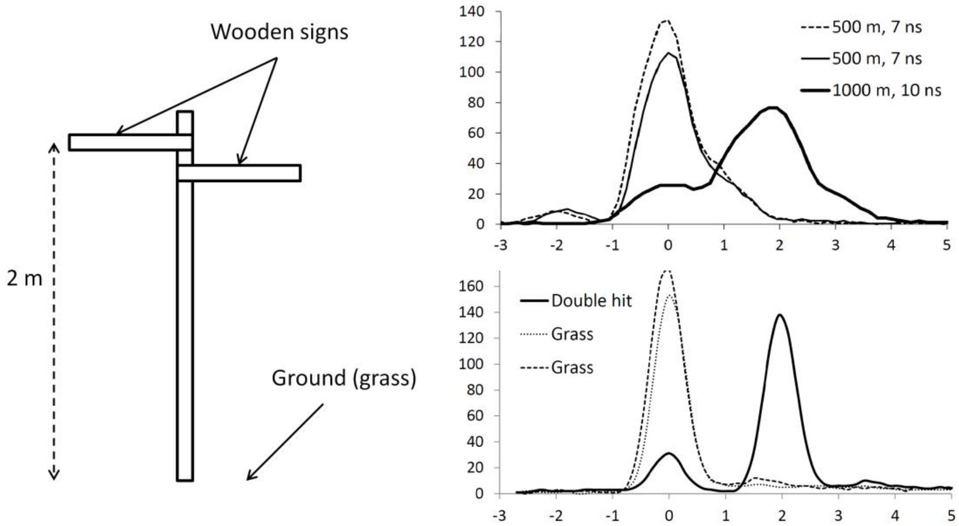

Figure 8. WFs of pulses (right) intersecting with a direction sign with 3–5 cm thick wooden signs placed 2 meters above the ground (left). The WFs are centered at the first echo detected by the DR circuit in the ALS60 or found by Gaussian decomposition of the WF in the LMS-Q680i. The unit of the x-axis is meters and y-axis shows the amplitude values. **Upper pulses:** ALS60 pulses from two acquisitions with system WFs of 7 and 10 ns in FWHM. All pulses produced one discrete echo. The 7-ns pulses show two peaks, but the first peaks at -2m were too weak to trigger an echo. In the 10 ns case, the two targets were confused. The discrete echo was detected from the leading edge of the pulse due to the constant fraction discriminator applied by the DR circuit.

Lower pulses: The sample pulses illustrate two single-echo cases from grass and a two-echo case in the LMS-Q680i data. The targets which are 2 m apart, are well-separated because of the shorter system WF (4.5 ns). All WFs show a ghost echo that has some 1.5 m of delay after the strong backscattering. There is also a general rise in the noise level that follows a strong reflection. The ghost echo in the LSM-Q680i is caused by a ringing effect.

2.4 Summary of estimation units and features

Each DR echo had the following attributes: coordinates (XYZ), height from ground (*h*), and intensity (*I*). An algorithm for processing WF data was developed in studies III and IV. The aim was to find meaningful noise-exceeding amplitude sequences (NEASs) and calculate WF attributes for them. First, the NEASs were extracted, i.e. the sequences that had at least five consecutive amplitude values clearly above an estimated noise level. Second, the entire WF was low-pass filtered with a Gaussian kernel (Hofton et al. 2000). Zero-crossings of the first derivative were used to detect peaks from the smoothed WF. The highest peak, maximum amplitude, was used to calculate the range and XYZ coordinates for the NEAS. Six attributes were calculated for each NEAS: peak amplitude (*A*), sum of the amplitude values i.e. the energy (*E*), full-width-at-half-maximum (*FWHM*), length (*L*), 50% energy quantile i.e. the center of gravity (*EQ50*), and number of peaks (N_{peaks}) (Figure 9).

Table 5 lists the features and estimation units applied in the studies. Individual pulses were examined in studies I, II, and III. Grid cells were used in study I, and vegetation samples (small trees or circular samples of low vegetation) in study III. Individual trees constituted the research objects in study IV, in which two methods for delineating the tree crowns were demonstrated. These were an automatic watershed segmentation algorithm, and manual treetop positioning (Figure 6) combined with a cylinder representing the tree crown. In the manual method, the maximal crown radius was predicted using allometric equations. The crown model in the manual method was similar to that in Figure 6 except that the crown radius was constant. The top 40% of the tree was always used in feature calculations.

Table 5. List of DR and WF attributes, and units of interest for which the features were calculated.

Study	Unit	N	Attributes	Distribution metrics
I	Individual pulse	-	*I*	-
	Grid cell (10×10 m)	66	*h*, *I*	Height percentiles, density metrics, deciles and moments of intensity distribution
II	Individual pulse	-	*I*, *A*	-
III	Individual pulse	-	*h*, *A*, *E*, *FWHM*, N_{peaks}	-
	Vegetation sample	7114	*h*, *A*, *E*, *FWHM*, N_{peaks}	Mean, SD
IV	Individual tree (watershed)	3630	*I*, *A*, *E*, *FWHM*, *L*, *EQ50*	Mean, SD, skewness, kurtosis, 1st–10th deciles
	Individual tree (manual)	9930	*I*, *A*, *E*, *FWHM*, *L*, *EQ50*	Mean, SD, skewness, kurtosis, 1st–10th deciles

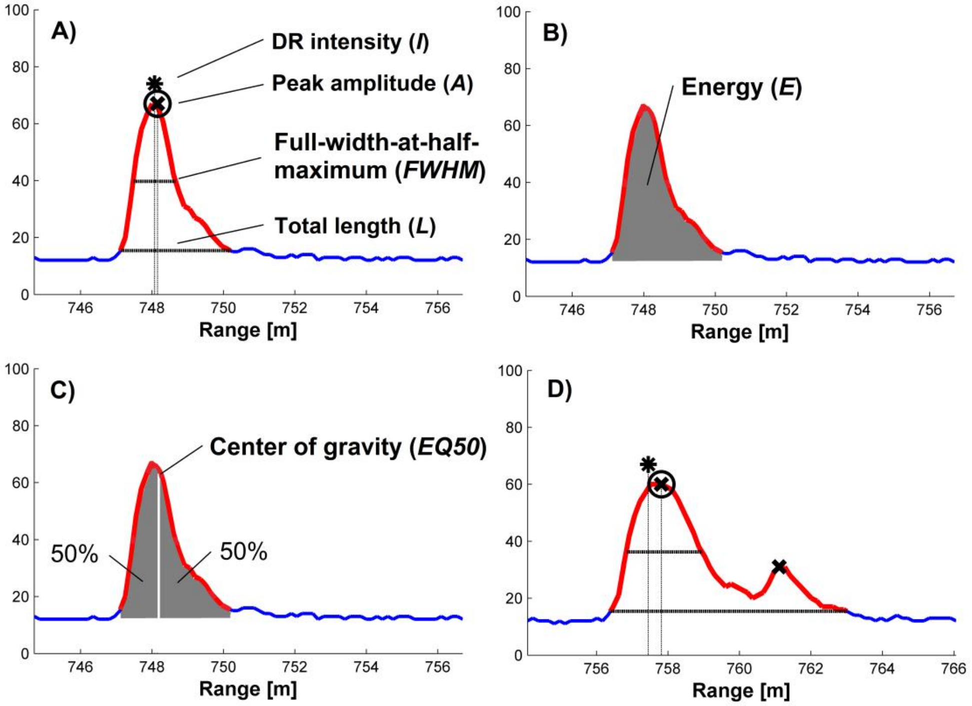

Figure 9. A-C: Attributes extracted from the noise-exceeding amplitude sequence (NEAS) of an ALS60 WF. **D:** Illustration of an NEAS with two peaks, in which *FWHM* was calculated for the main peak, and *L* was calculated for the entire NEAS. The vertical lines depict range values for the DR echo and for the peak amplitude of the WF.

2.5 Radiative transfer modeling

2.5.1 Overview

Radiative transfer modeling was used in studies I and III. The approaches differed in the level of detail of vegetation representation and calculations. Simple rotationally symmetric crown models and the Beer-Lambert law were applied in study I, whereas geometric-optical models resolving the vegetation structure at leaf-level were used in study III. Also, the pulse paths in the canopy were traced in study I, while the paths of individual photons were sampled by Monte Carlo ray tracing (MCRT) in study III. Next I describe the vegetation models followed by an explanation of the ray tracing approaches used.

2.5.2 Geometric-optical models of vegetation

The crown envelopes and stems of individual trees were modeled in study I. The maximum crown radius was predicted using species-specific allometric equations derived from field data, using h and d_{13}, or h alone as independent variables. A curve of revolution was used to describe the crown radius between the tree top and 60% relative height. A cylinder defined by the maximum crown radius was used to model the crown below the 60% limit. The crown base height was measured for a majority of the overstory trees and modeled for the understory trees. The stem form was modeled as a truncated cone. An assumption of turbid media within the crown was made when modeling the transmission losses with the Beer-Lambert law.

Geometric-optical models that resolved the vegetation structure at leaf-level were constructed in study III. Models were built for birch, raspberry and fireweed. The 3D structure of birch was modeled using an empirical model by Lintunen et al. (2011). In the model, a set of regression equations predict local crown characteristics recursively on the basis of local predictors and tree-level input variables such as tree *h*, crown length, d_{13}, and the degree of between-tree competition. The 3D structure of first-year raspberry and fireweed shoots was based on field measurements of shoot and leaf dimensions, and regression models fitted to these data. The models explained the number, size and positions of the leaves along the shoot. For all species, the regression models gave the overall structure of the canopy. To obtain the leaf shapes, sample leaves were digitized. The leaf size was scaled to match the leaf area predicted by the regression models. The total leaf area for birch was given directly by regression equations. The total leaf area of raspberry and fireweed canopies was obtained by adjusting the number of shoots per square meter in order to achieve LAI values which are found in the literature (Kuusk et al. 2004). To obtain leaf orientations, theoretical leaf angle distributions were used (de Wit 1965; Weiss et al. 2004). A spherical distribution was used for birch and a planophile distribution was used for raspberry and fireweed. The selections were based on field observations. Directional-hemispherical reflectance and transmittance factors measured for birch leaves (Lukeš et al. 2013) were used as reflectance and transmittance values for the leaves of all species. The reflectance properties of the shoots were assumed to match those of leaves in raspberry and fireweed. The reflectance of birch branches was adopted from literature. Zero transmittance was assumed for all shoots, and for birch branches and trunks. The ground was modeled as a Lambertian horizontal plane with a reflectance that corresponds to an average determined for mosses (Lang et al. 2002).

2.5.3 Monte-Carlo ray tracing simulation model

The LiDAR simulation model in study III was based on a mathematical formulation of the LiDAR signal:

$$V_o(t) = P_e(t) \times \eta_{atm} \times \frac{1}{A} \otimes \sigma(t) \times \eta_{atm} \times \frac{\pi D^2}{4R^2} \otimes \Gamma(t) \times g + c \tag{6}$$

where $V_o(t)$ is the voltage recorded by the receiver [unitless], $P_e(t)$ the emitted power [W], η_{atm} the atmospheric attenuation factor [unitless], A the target area [m^2], $\sigma(t)$ the target differential scattering cross-section [m^2 sr^{-1}], D the receiver aperture diameter [m], R the scanning range [m], $\Gamma(t)$ the receiver response function [unitless], g the receiver gain (scaling factor) [W^{-1}], and c noise [unitless]. The symbol × denotes multiplication and ⊗ convolution. The constant terms are embedded into the system WF ($S(t)$):

$$S(t) = P_e(t) \times \eta_{atm} \times \frac{1}{A} \times \eta_{atm} \times \frac{\pi D^2}{4} \otimes \Gamma(t) \times g \tag{7}$$

Thus, the final equation may be simplified to:

$$V_o(t) = S(t) \otimes \sigma(t) \times \frac{1}{R^2} + c \tag{8}$$

meaning that the LiDAR signal comprises of system waveform ($S(t)$), target differential scattering cross-section ($\sigma(t)$), scan range (R), and an additive noise term (c). $S(t)$ can be solved using well-defined planar surfaces of accurately known reflectance, i.e. calibration targets.

The retrieval of $\sigma(t)$ required a method for modeling the photon transport in the canopy. Due to the detailed nature of small-footprint LiDAR measurements, the method applied must be able to handle arbitrarily complex scenes (Calders et al. 2013). Therefore, the Monte-Carlo ray tracing (MCRT) method was chosen. MCRT is commonly acknowledged as one of the most accurate methods for RT modeling, against which simpler models are tested (Widlowski et al. 2008). The assumption in MCRT, as in any model based on radiative transfer theory (Chandrasekhar 1950), is that the wave phenomena due to the coherent nature of the laser light can be ignored. The issue was discussed by Wagner (2010) who concluded that despite the theoretical considerations, radiative transfer theory may be accurate enough for modeling the scattering of laser light in practice. The MCRT model was implemented in Java programming language. It functioned in a forward mode, i.e., the photon paths were sampled from the transmitter towards the receiver (e.g., Disney et al. 2000). A Gaussian spread of irradiance across the laser footprint was assumed and although the model could simulate an infinite number of scattering orders, they were constrained to the first ten.

2.6 Statistical methods

The analyses included classification of individual LiDAR pulses, vegetation samples, or trees in studies I, III and IV. Because the number of classes was small and the purpose was to study the potential discriminative power of LiDAR features, linear discriminant analysis was considered sufficient in studies I and III. Quadratic discriminant analysis was used in study IV to account for the differences in variance-covariance structure between classes. Overall accuracy (correct-%), producer's accuracy (correct-% per class) and Cohen's kappa (κ) were used to evaluate the results as:

$$Correct-\% = \frac{TP}{TP + TN} \times 100 \tag{9}$$

$$\kappa = \frac{P(o) - P(e)}{1 - P(e)} \times 100 \tag{10}$$

In Equations 9 and 10, *TP* is the number of true positives, *TN* is the number of true negatives, and *P*(*o*) and *P*(*e*) are the observed and expected probabilities for correct classification, respectively.

Ordinary linear regression analysis (linear models) was used frequently to characterize the dependencies of the studied features on independent variables such as vegetation characteristics. In study IV, a linear mixed-effect model (LME) was used (McCulloch et al. 2008). In LME, the response of variable y is explained by continuous or categorical predictor variables x, which can be either fixed or random. The fixed variables are treated similarly as in ordinary linear regression, in which the coefficients for x are estimated from the data, and they tell how y is influenced by x in the data examined, under specific assumptions. The coefficients for the random x on the other hand, differ in their interpretation. They are random realizations from the entire population. In study IV, the idea was to model the dependence of LiDAR features on the independent tree and acquisition parameters. Individual trees were samples from the entire population and therefore the mean difference of each tree from an average tree (the 'tree effect') was considered as a random realization from the population of trees.

3 RESULTS

3.1 Geometry and radiometry of DR measurements in the understory (Objective I)

The key component in study I was a ‘real world ray tracing analysis’, in which individual echoes and pulses of discrete-return data were linked with accurately positioned tree objects that were modeled for crown shape. Echo triggering probabilities and intensity measurements in the understory were examined in this setup. In addition, the performance of area-based LiDAR features was tested for predicting the characteristics of the understory tree layer.

The most important findings of study I considered transmission losses in the upper canopy. It was empirically shown how transmission losses reduce the echo triggering probability and intensities measured for the understory (see explanations in Figure 10). It was further verified that ‘low-SNR losses’ exist, i.e., transmission losses due to weak backscattering that is not recorded as the reflected energy remains below the detection threshold of the sensor. The intensity data was deemed of low value for the identification of understory tree species at both the individual pulse level and in area-based analyses, even when using first-or-only returns that are less influenced by losses. In spite of the discouraging results, a correction of the second-return data for transmission losses was attempted. It was shown that the separability of ground echoes and those from the most abundant tree species was improved, however, the classification performance remained lower than that seen in first-or-only return data.

Many findings related to the effects of tree structure and sensor characteristics were seen in study I. Tree species, pulse position within crown, and the size of the understory were shown to affect the echo-triggering probabilities. The density of the small understory trees and the relative position of the pulse within crown exercised an effect on the intensity values. All of these findings were in agreement with the LiDAR theory (Equation 2) and confirmed the good geometric match of LiDAR and field measurements. Differences in the intensity recording between sensors (Optech ALTM3100 and Leica ALS50-II) were observed in the single-return data.

The area-based LiDAR features showed some potential for the detection of understory trees, despite inherent selection towards targets of high backscatter cross section (reflectivity, density, geometry) due to transmission losses. Particularly, the proportion of ground returns explained the number of understory trees per hectare ($R^2 = 0.55–0.87$). The results for mean understory tree height were however not as good ($R^2 \leq 0.51$).

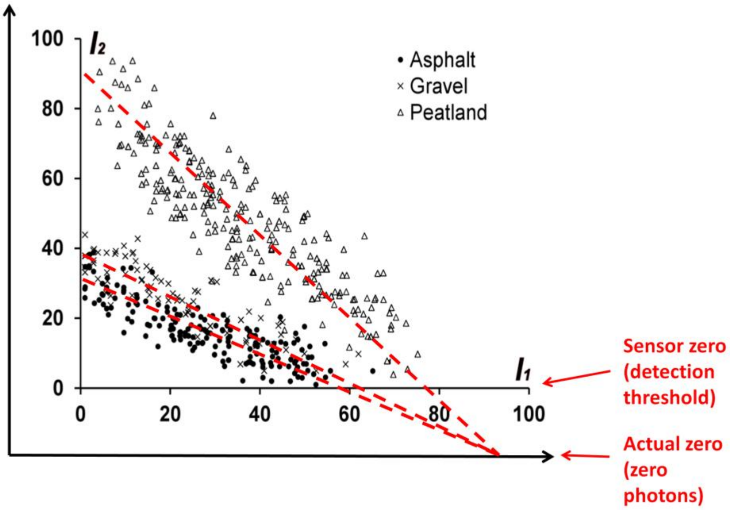

Figure 10. Illustration of the effect of transmission losses on echo triggering probabilities and intensity measurements. The scatterplot has DR intensities of two-echo pulses, in which the first echo (I_1) is from a pine canopy, and the second echo (I_2) is from well-defined surfaces of varying reflectance: asphalt, gravel and peatland. The reflectance and geometric properties of pine crowns are assumed to be stationary, and I_1 is assumed to depend mainly on silhouette (projection) area. Thus, I_1 measures transmission losses, and for a given surface, I_2 is inversely proportional to I_1. The digital 8-bit intensity scale starts from 'zero'. However, this does not correspond to 'zero backscattering'. Instead, the recorded zero corresponds roughly to the detection threshold of the receiver's DR circuits, which differ for each return number. If I_1 is high enough, there is not enough energy left for a second triggered echo. This 'no-second-echo' threshold depends on the ground reflectance. For example, it is ~50 for asphalt (reflectance ~0.15–0.2), and ~80 for a bright peatland surface (reflectance ~0.4). The data is taken from an ALTM3100 sensor.

3.2 Close-range photogrammetric observations of canopy in explaining LiDAR backscattering (Objective II)

It was shown as feasible to accurately orientate a block of upward-looking terrestrial images into the coordinate system of the LiDAR data. The dense network of image locations enabled viewing some of the pulses as almost collinear, so that intersected targets could be outlined in the images. The branch silhouette areas filling the footprints were calculated, using binarized images. Improvement of the planimetric match between images and the individual LiDAR strips was even made possible by shifting the LiDAR data in XY and searching for XY-shifts that maximized the correlation between the LiDAR intensity and the silhouette area. The complex problem of image binarization was optimized simultaneously. The planimetric shifts at strip level were below 0.3 m, which were in line with other observations in the study area (Korpela 2008). Of course, a part of the observed mismatch was due to errors in the image block orientation.

DR intensity and WF peak amplitude served as measures of LiDAR backscattering in the isolated branches that were purposely selected to represent 'shallow targets'. The

Pearson correlation coefficients in the pine stands ranged from 0.5 to >0.9 suggesting that the silhouette area could explain over 80% of the variance in backscattering. In the dense spruce stand it was more difficult to find suitable pulse-branch cases for the analyses, and the correlation coefficients were lower (0.4–0.8). The observations were probably also noisier due to occlusions, and spruce branches may actually exhibit more variation due to their shoot and needle geometry and epiphyte lichens. ‘Pseudoechoes’, i.e., footprints of pulses that had not triggered an echo at a certain height were analyzed for cases in which the pulse path traversed close to branches, in order to determine the minimum echo-triggering silhouette. The remaining small geometric inaccuracies in both the LiDAR data and the images prevented very accurate conclusions from being made. Nor could it be clearly shown using the branch silhouette estimates, that the footprint irradiance had a Gaussian spread, although it was more obvious in analyses using power line cables. Overall, it was shown that the photogrammetric method was useful for making qualitative observations about the pulse interactions with forest canopies, and the visualizations of WF data using this approach were also very educative.

3.3 Comparison of simulated and real WF measurements (Objective III)

A LiDAR simulator that was based on MCRT was developed and validated in vegetation against real data. The validation was preceded by calibration of the simulator using horizontal well-defined targets that had been measured for hemispherical-directional reflectance. The simulator could be used with three common species: birch, raspberry and fireweed. Geometric-optical models of these were constructed and a large number of georeferenced field samples were made available. The validation was performed by simulating observations with scan geometry equivalent to the real data, and by comparing the mean and standard deviation of selected WF attributes and echo heights against those in the real data. The sensitivity of the simulation results to the vegetation parameters was investigated and the results were qualitatively compared against real observations to ensure that the simulator functioned logically.

Validation showed good agreement between simulated and real data, particularly in the WF attributes (Figure 11). The echo height histograms (echo height from ground) showed small discrepancies, probably caused by geometric inaccuracies in the vegetation models as well as minor imprecisions in the implementation of the CFD algorithm. The effects of footprint size could be correctly simulated. The sensitivity analyses showed that leaf angle distribution strongly influences backscattering, while reflectance and leaf area have a lesser role. It was also shown that 2^{nd} or higher order scattering can considerably contribute (12–43%) to the total signal in birch and raspberry canopies. Furthermore, the contribution of photons scattering from 'outside' the $1/e^2$ footprint (relative distance of 136% from the footprint center) was approximately 20%. The latter was observed in dense raspberry canopies, in which the photons do not escape the scene immediately following the first interaction.

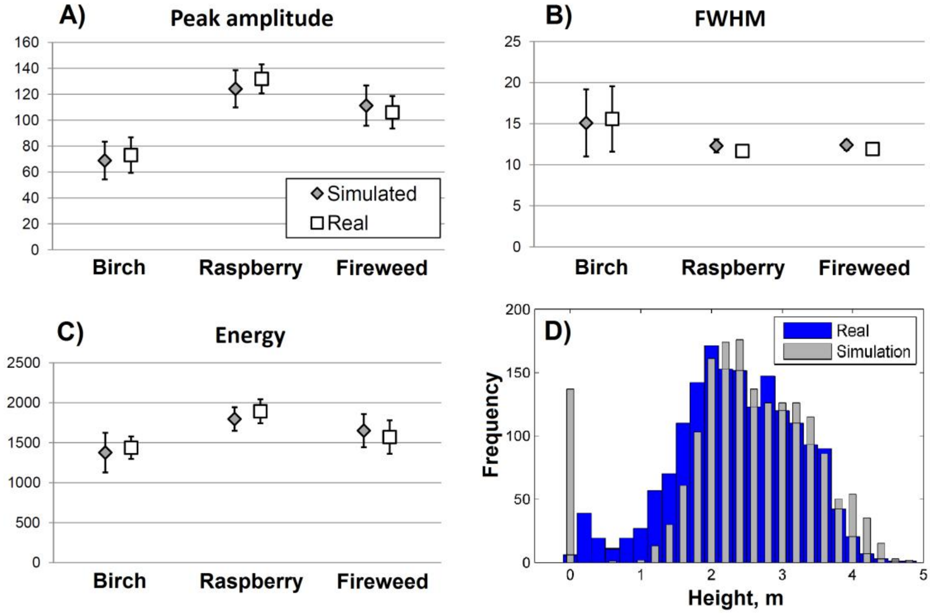

Figure 11. Comparisons of simulated vs. real LiDAR data. **A–C:** Boxplots of peak amplitude, FWHM, and energy attributes for birch, raspberry, and fireweed canopies in 2012 - 1 km data. The whiskers denote standard deviation. **D:** Height histogram of DR echoes of birch in 2010 - 1.2 km data. The echoes were detected by a constant fraction discriminator algorithm.

3.4 Effects of vegetation, sensor and acquisition properties on WF features (Objective IV)

Studies II and III provided fundamental information on how WFs are affected by the geometric-optical properties of vegetation, at the scale of individual pulses. Study IV focused entirely on the empirical analysis of vegetation, sensor and acquisition parameter related effects on the WF attributes and features, at pulse, and individual tree scales. These questions were also partly examined in study III. Additionally, the simulator was used in study III to investigate different sensor effects. The empirical analyses were performed using Leica ALS60 data.

The backscattering of different tree species and low vegetation canopies of young forests were investigated in study III. The units of interest were individual pulses and small circular vegetation samples. Results showed that WFs are influenced by footprint-scale structure and reflectance characteristics. Figures 12 and 13 show some results in raspberry canopies that were measured for LAI and h. These extra validation data were not included in study III. However, figures 12 and 13 further confirm the results in study III concerning the response of the LiDAR signal to leaf area, which in study III were based on less reliable and subjective ‘canopy cover’ estimates. Furthermore, the average LAI in the samples measured was 3.16 - a value close to the literature value of 3.35 which was used in the simulations.

Figure 12. Examples of raspberry canopies with low and medium leaf area index.

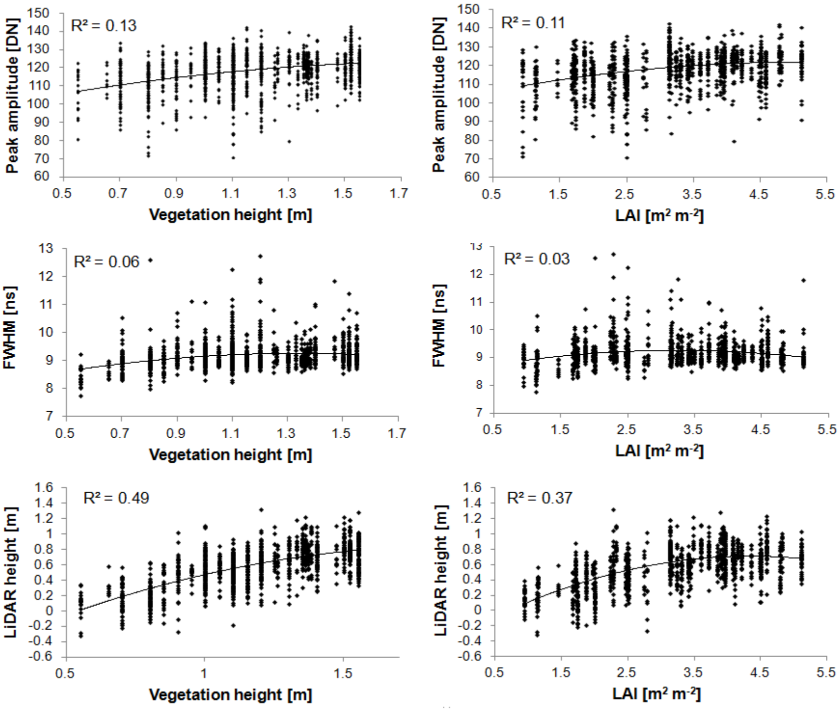

Figure 13. Dependence of field measured maximum vegetation height and LAI (m^2 m^{-2}) with the peak amplitude, FWHM, and echo (NEAS) height in raspberry canopies. The dots represent pulse NEASs that had intersected the vegetation samples. The NEAS height from the ground was obtained by calculating the XYZ coordinates at the peak amplitude, and subtracting the GNSS measured ground elevation.

In study III, it was shown that four vegetation functional groups of seedling and sapling stand vegetation could be classified reasonably well using WF attributes. For example, the low vegetation associated with barren site types that comprise low LAI and height (c.f. Figure 13) could be separated from more ‘vigorous and green’ vegetation. Pine could be separated from the other tree species, but spruce did not differ well from broadleaved trees in WF attribute data.

The influence of sensor parameters on WF data was studied by simulation in study III. The most important finding was the effect of footprint size on the species classification performance, which was further supported by analysis with real data. The conclusion was that footprints smaller than 0.3–0.36 m in diameter should be avoided in the pulse-level classification of low vegetation. A larger footprint averages out the irrelevant small-scale spatial variation of vegetation, which improves classification at the pulse level. Emitted pulse width and the digitization rate did not affect the separability of species in simulations using WF attributes.

Study IV was about the effects of species, other tree-related parameters, and acquisition characteristics on the WF features of trees older than 25 years. The basic estimation units were individual trees. Descriptions and explanations for between- and within-species differences in the WF features were provided by the analyses. The magnitudes of various effects on the features were evaluated using LME models. The energy of only returns turned out to be a superior predictor of tree species. Non-quantified (or ‘difficult-to-quantify’) between-tree structural differences, i.e. the tree effect, explained a majority of the within-species variation suggesting that species separability is limited when using the features and the type of forest studied. However, the correlation of the tree effect between features was not examined. Illustrative findings were made on how stand-specific characteristics, crown status and vigor as well as branch morphology influence the features. These provide possible explanations for the tree effect. Of the fixed (known/measured) predictors, tree height and/or age affected all of the features (Figure 14). The effects of scan zenith angle and phenological status offered unique findings. Although small in magnitude, these effects imply possibilities for fine-tuning species classification algorithms by well-thought data acquisition. Increasing the scan zenith angle from 5° to 15° increased the peak amplitude of spruce and birch by 4–9%. The early summer (June) LiDAR acquisition proved beneficial for providing WF data that separates pine from other species. The new needle cohort in pine was not fully developed in June, and thus the needle mass or LAI was lower when compared to late summer. Early summer WFs from pine showed lower energy. Site type had a minor effect on feature variance in our data although exceptional sites such as barren pine bogs offered some deviation. Finally, the dependence of the residual, i.e. random variance on the number of pulses per tree was modeled. The variance of the energy (E) of only returns was most insensitive to a reduction in the number of pulses, which has important implications concerning the potential operational use of E in low sampling-density WF data. Division between return types (only/first-or-only) was important also because the only returns were least sensitive to within-species structural differences and occurred on average closest to tree trunk, which explains why they were particularly superior in species classification when the crown delineation was inaccurate.

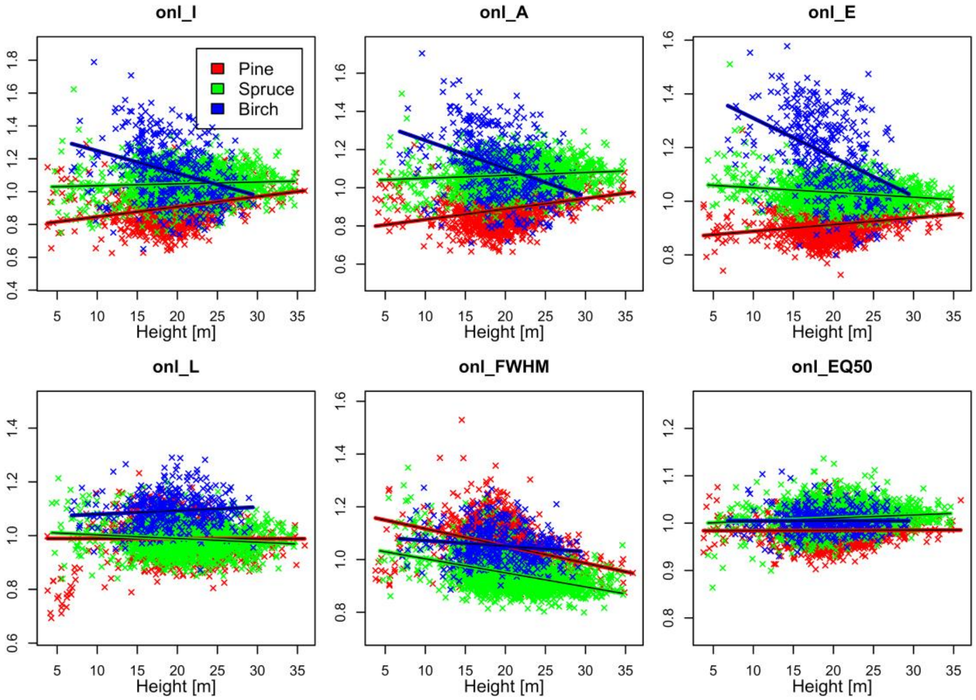

Figure 14. Influence of tree height on tree-level mean WF features (mean of WF attributes per tree crown) calculated from only returns in 2013 LiDAR data (700 m flying height). The lines represent univariate regression models fitted separately for each species.

3.5 Classification results using WF data (Objective V)

The four vegetation functional groups in seedling and sapling stands were coniferous trees, broadleaved trees, ‘barren and low’ vegetation, and ‘green’ vegetation. They were classified in study III at the level of individual pulses, and vegetation samples that could comprise several pulses. The results were benchmarked with an earlier study that utilized multispectral aerial images and DR LiDAR data (Table 6). This was also done in Hyytiälä in similar vegetation (Korpela et al. 2008). The comparison is slightly impeded by the fact that the classes and the balance and amount of data differed slightly in study III.

Tree species were classified in study IV and the results were evaluated against a set of DR intensity features that were proven useful in another study by Korpela et al. (2010b) that was also conducted in Hyytiälä (Table 6). The results reported in Table 6 were obtained by including moments and deciles of the WF attributes as candidate features in feature selection and classification. Correct-% was reduced by up to 2.6 percentage points (κ by up to 0.04) when using only the mean values of WF attributes per tree crown as features. Independent on the feature set applied, watershed segmentation resulted in higher classification performance compared to manual delineation method. Majority of the difference could be attributed to watershed tree set representing a sample that deviated slightly in its characteristics from the entire population of dominant/co-dominant trees. The delineation method did not therefore influence the classification performance. However, different delineation methods resulted in differences in the best-performing WF feature combinations.

Table 6. Summary of classification accuracies achieved with WF data.

Study	Unit	Correct-% (κ), in benchmark data	Correct-% (κ), WF data
III	Individual pulse	-	68–87 (0.51–0.80)
III	Vegetation sample *	61–79 (0.44–0.67) *	74–85 (0.52–0.79)
IV	Individual tree (watershed)	78–89 (0.64–0.82) **	88–95 (0.79–0.91)
IV	Individual tree (manual)	74–85 (0.57–0.75) **	84–91 (0.74–0.86)

* Not fully comparable. Slightly different classes and numbers of observations per class than in Korpela et al. (2008).

** Using the intensity features as defined in Korpela et al. (2010b)

4 DISCUSSION

4.1 Pulse-level properties of empirical LiDAR data (Objectives I and II)

The accurate field measurements and positioning of the trees in relation to the LiDAR coordinate system in study I made it feasible to assign pulses and echoes even to small trees. Furthermore, the LiDAR sensor trajectories were available, which enabled tracing of the pulse paths or vectors within the canopy. Thus, it was possible to understand the observations better, compared to using DR point data alone, which was typical for LiDAR studies at the time. However, it became obvious that DR sensors obscure much of the information about backscattering. Some of the findings of study I may therefore seem obvious based on the later knowledge gained from WF data analyses. For example, the intersensor differences in near-ground intensity recordings may be due to the echo detection algorithm. The ALS50-II applies constant fraction discrimination for ranging and the intensity is the instantaneous amplitude at that range. The ranging or intensity recording methods that are implemented in ALTM3100 are however unknown.

Transmission losses were shown to reduce echo triggering probability, which skews the distribution of second echoes towards highly reflective targets (high value of apparent backscatter cross-section). Both effects were caused by the same phenomena: with increasing transmission losses, a higher number of reflections remain below the triggering threshold of the sensor. At a fixed level of transmission losses, the less reflective (less dense or unfavorably oriented) the target, the higher is the probability that the signal remains below the triggering threshold. It was hypothesized that the same problem holds true in WF data because thresholding is needed in WF processing to exclude irrelevant noise. However, when WF storage has commenced the data shows weaker backscattering than would be needed to trigger the storage. In our data, the ALS60 sensor saved 256 samples independent of the amplitude data, while the LMS-Q680i would stop after 80 or 160 samples if the signals were low. Hence, the issues related to triggering may constitute a bigger concern in LMS-Q680i data. The documentation of ‘low-SNR losses’ was important and further illustrated how DR data lack details. Yet again, WF sensors apply a threshold that triggers the WF recording, in order to save data transfer and storage capacity. Thus, the ‘low-SNR losses’ may be present in WF data also. For these reasons, it would be interesting to repeat study I using WF data. Finally, the introduction of an offset term to the intensity measurements was an important contribution, as it brought the intensity observations closer to ratio scale. However, as shown in study IV, the receivers in Leica ALS50/60 sensors do not provide intensity data in linear scale and the offset is only an approximation. To my knowledge, the use of an offset term has not been covered in earlier studies dealing with intensity calibration (e.g. Ahokas et al. 2006; Wagner et al. 2006; Höfle and Pfeifer 2007; Korpela et al. 2010a; Gatziolis 2011). The offset is of course sensor/circuit-specific, and our method of measuring it using two-echo pulses (Figure 10) was not optimal. However, it was the only conceivable option available at the time.

Despite the correction for transmission losses, the information value of second return intensity data was low. This was partly because of the aforementioned skewing of the target population. It also became evident after the WF analyses in studies III and IV, that the intensity data measures the pulse energy only when the target is not extended. Thus the correction model was based on inadequate data. To illustrate this, Figure 15 presents 2nd return intensity plotted against 1st return energy calculated from the WF data.

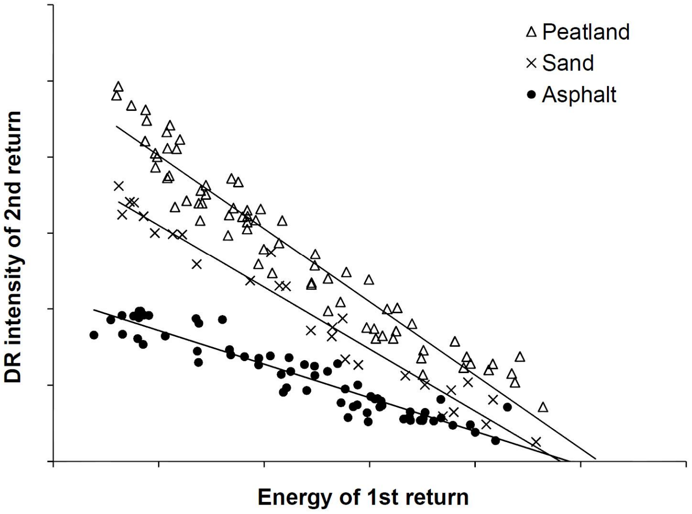

Figure 15. DR intensity of the 2nd echo plotted against energy of 1st echo (NEAS). The 1st echo is from the pine canopy, and the 2nd echo stems from well-defined surfaces of varying reflectance (cf. Figure 10). The R^2 values are over 0.88 in all surfaces, whereas the R^2 values when using DR intensity alone were 0.67–0.77 (Figure 10). These figures indicate that energy is a better measure of transmission losses, compared to DR intensity. The data is from 2012 ALS60 acquisition and normalized in order to make data from separate flying heights (1–2.7 km) comparable. An offset term is added in the normalization, and thus the regression lines intersect at approximately zero. The data from the 0.5 km flying height showed lower R^2 values. It is probable that the small-scale variation in reflectance and/or orientations of scatterers averages out when using larger footprints.

Some authors have studied the issue of transmission losses in WF data after study I was published. Success was evaluated by the performance of area-based predictions of vegetation volume (Lindberg et al. 2012), or by visual examination of the voxel-based canopy representation (Richter et al. 2014). The results indicated that correction for transmission losses could improve area-based estimates of the forest vertical structure and understory. In addition to transmission losses, one has to also consider the inadequate sampling of the understory trees in the LiDAR data because of occlusions, and statistical methods are therefore required to compensate for the incomplete observations.

The operational context of study I was the mapping of understory trees, and this has gained the attention of only a few studies (Maltamo et al. 2005; Hill and Broughton 2009; Martinuzzi et al. 2009; Morsdorf et al. 2010; Jaskierniak et al. 2011). Our small scale tests using the area-based approach showed that DR data has potential for predicting the abundance of understory, i.e. for making decisions about pre-harvest clearing or for the assessment of important habitats. The results for mean understory tree height were not as promising, probably because the heights of the understory trees were highly variable. Therefore, the arithmetic mean height of trees was probably not the best possible characteristic by which to describe the vertical distribution of leaf area which ultimately determines the height distribution of LiDAR returns (Magnussen and Boudewyn 1998). The highest understory trees may also have been confused with the upper canopy layer. Leiterer et al. (2013) have shown that multitemporal leaf-off/leaf-on data may be required in the presence of very dense upper canopies. Overall, the representativeness of the test sites was quite limited and further studies will help to generalize the results.

Study II aimed at linking ratio-scale within-footprint vegetation characteristics with LiDAR measurements. Very few studies have been published on the subject (Doneus et al. 2010). This is understandable because a method to measure the details of the vegetation must be available, and an accurate geometric match between the reference and LiDAR data is needed. Our photogrammetric method can be carried out using inexpensive consumer-grade digital cameras. The images are easily visualized and individual scatterers could be identified along the pulse path, which was very interesting. Multiple views could be used to position targets in the canopy. Beyond the results presented in II, the photogrammetric method has already proven useful for analyzing the geometric accuracy of the LiDAR strips and for visualizing the LiDAR WFs from different targets (Figures 6 and 8). An example of the use of the method could be the analysis of the quality of LiDAR point clouds for detailed 3D feature extraction (Li et al. 2013). It is known that the echo detection method applied may substantially influence the echo coordinates (Wagner et al. 2004). An alternative is the use of terrestrial laser scanning (TLS) (Pfeifer et al. 2004; Côté et al. 2009). The benefit of TLS is the direct retrieval of a 3D point cloud. Occlusions are a more serious issue in image data and complex canopies that occur in depth constitute very difficult targets for triangulation by automatic or manual image matching. The difficulties in the application of both photogrammetry and TLS are related to the EO of the image block, because no man-made targets for co-registration are usually available in the forest. We used a large number of treetops (trunks) measured photogrammetrically in aerial images. GNSS control points measured in open areas are an alternative, but the geometry needs to be brought to the site of research by means of field triangulation. As an additional consideration, windy conditions should be avoided during LiDAR acquisition and canopy photogrammetry because tree sway can be substantial (cf. Korpela 2004).

Besides testing the photogrammetric method, the aim in study II was to empirically test the LiDAR theory (Wagner et al. 2006; Wagner 2010) by linking the within-footprint silhouette area with the LiDAR backscattering, in the presence of limited variation in target reflectance and geometry (the two other components of backscatter cross-section). A potential application where this knowledge could be utilized is the improvement of canopy cover estimation from LiDAR data (Korhonen et al. 2011). Multi-echo pulses have to be handled in the canopy cover estimation formulae. Solberg et al. (2009) made a 50% canopy cover assumption for multi-echo pulses. With the image data, this threshold could be more accurately determined and even an exact relation between LiDAR intensity (or the energy of the WF) and canopy cover could be determined (Hopkinson and Chasmer 2009). For this purpose, calibration data are needed in order to quantitatively link the projected leaf area with the silhouette area measured in the thresholded binary images. However, aspects related to image acquisition and binarization (e.g., light conditions during the acquisition) pose challenges to realizing this application.

4.2 Usability of the MCRT simulator (Objective III)

Study III summarized the lessons learned in studies I and II by embedding the many aspects into an MCRT simulation model. Overall, the simulated data agreed well with the real observations of the three species studied. Comparisons of simulated and real data have previously been reported for spaceborne LiDAR (North et al. 2010). Compared with for example passive multispectral RS, it became obvious that the implementation of the LiDAR simulator was easier since the target illumination is highly directional and the backscatter view-illumination geometry is relatively simple to model. In passive imaging one has to consider the directional and spectral variation of solar illumination which includes diffuse sources, varying view geometry, as well as prominent atmospheric effects in the visible range bands. The increased availability of WF recording LiDAR sensors makes simulator validation efforts easier as it is not necessary to simulate the echo triggering method (Disney et al. 2010), although the triggering of the WF recording must still be simulated. Our study was among the first to compare real and simulated small-footprint LiDAR data.

Comparisons to real data are typically limited by a lack of knowledge of the receiver's functioning and the need for realistic and representative parameterizations of the vegetation (Roncat et al. 2014b). We solved the combined effect of the emitted pulse and the receiver response (i.e., the system WF) empirically, using calibration targets. The simulated vegetation was purposefully chosen to represent relatively simple structures. The structural similarity of the simulated vegetation with real counterparts was verified even by visual examination. Both the structural simplicity and the fact that the optical properties of plant leaves do not generally vary much by species at 1064 nm (Walter-Shea and Norman 1991; Hosgood et al. 2005), simplified the efforts towards geometric-optical plant modeling. Despite good results in the simulator validation, there were still some experimental uncertainties, as well as issues in simplifying assumptions in the modeling of the vegetation, in calibration targets, and in the modeled receiver response. These aspects warrant critical evaluation.

It is obvious that there were geometric discrepancies between the modeled and real vegetation as shown by the slightly differing height histograms of real and simulated echoes. The optical properties of the simulated vegetation could have been modeled more accurately, but such backscatter reflectance data does not generally exist for coherent light, and because of the difficult observation geometry involved. In addition to the directional-hemispherical reflectance and transmittance factors and the Lambertian assumption on directional reflectance, it would be advantageous to have measurements on the true directional characteristics of the reflected/transmitted radiation for accurate simulations (see definitions of reflectance quantities in Schaepman-Strub et al. 2006). Assumptions about the leaf angle distribution were made based on visual assessment in the field. Minor tests with the birch saplings were made after study III was published, using a method that applies photography (Pisek et al. 2011). The results suggested that the LAD of birch resembles that of a spherical LAD, which was assumed in the simulations. The hemispherical-directional reflectance factor (HDRF) of the calibration targets was determined by field goniospectrometer measurements (Suomalainen et al. 2009), and nadir HDRF measurements with a 47–60 degree phase angle were used as reference for the calibration, although such HDRF data do not correspond to the highly directional LiDAR backscatter geometry (Kaasalainen et al. 2005). The linear behavior of the receiver was assumed, i.e., the linear response of the amplitude values to instantaneous power entering the receiver. Later analyses (involving multi-height data from well-defined surfaces with fixed transmitter and receiver settings, contrasted against the radar equation) have shown that in our ALS60, the response of the WF peak amplitude is slightly non-linear. It also shows that the receiver response function changes somewhat depending on the strength of the signal, which distorts the shape of received WFs of different strength (study IV). In study III, the calibration targets and the vegetation samples were both highly reflective and did not cover the low-end of the measurement scale, which explains why the linear model sufficed.

The drawback of complex MCRT models is that the results may be difficult to interpret and that the models are difficult to parameterize (Disney et al. 2000). Realistic parameterizations are needed at all levels of detail (cf. Figure 1). The focus in study III was on the WF attributes, which are mainly affected by small-scale variations in the structure and optical properties of objects that are visible to the receiver and contribute to the signal by N-order scattering. It is obvious that in mature trees the spatial distribution of the scatterers within tree crowns must be modeled in a way that realistic data can be simulated, for instance to derive the correct height distributions of echoes (Calders et al. 2013). Geometric-optical modeling of conifers is generally more difficult compared to modeling broadleaved trees. Firstly, modeling the reflectance and transmittance of thick needles that taper and are asymmetric is problematic. Furthermore, the spatial arrangement and orientation of needles in shoots is difficult to model realistically, and errors will have an effect on the simulation results (Disney et al. 2006; Smolander and Stenberg 2003). Therefore, it may be advisable to use a shoot as a basic unit in simulations, at least when they are easily definable, as in the *Pinaceae* species (Smolander and Stenberg 2003; Morsdorf et al. 2009; Mõttus et al. 2012). Overall, a high level of detail is needed in geometric-optical models that are used in LiDAR simulators (Roncat et al. 2014b). One must also consider the representativeness of the plant models with respect to the variability of real populations. The optical properties of individual leaves or needles can be measured to some extent with coherent light and in their backscattering geometry (Kaasalainen and Rautiainen 2007), and the high-level structure can be modeled through e.g., TLS measurements (Pfeifer et al. 2004; Côté et al. 2009; Raumonen et al. 2013). However, the results concerning inter-tree variation in study IV suggest that trees are highly variable and our understanding on how to treat this variability of geometric-optical properties requires further research efforts.

In regard to model validation, we can say that vegetation field measurements are extremely laborious. It may therefore be more feasible to determine critical simulator components by entirely theoretical studies, where the influences of simplifying assumptions and uncertainty in MCRT model parameters are examined by comparison with benchmark simulations that have accurate models (Widlowski et al. 2008; Widlowski et al. 2014). The accuracy requirements for the simulator, as well as the computational effort, depend on the estimation unit (pulse→tree→stand), and also the application which is envisaged. According to Widlowski et al. (2014), one has to set predefined standards for the accuracy required, and then evaluate the simulation results based on those standards.

Despite the difficulties in model parameterization and validation, I believe that use of MCRT and detailed vegetation models will increase in the future. MCRT model computations can be parallelized so that their computational power is consistently increasing and may no longer pose the limiting factor that was present in many applications up until a few years ago. Memory consumption may be a problem, at least when creating very detailed and realistic models such as entire forest stands in which individual trees exercise variation in their characteristics.

4.3 WF features and their use in classification (Objectives IV and V)

As shown in studies II and III, LiDAR measurement is affected by small-scale geometric-optical characteristics of vegetation that include leaf angle, leaf projection area and optical properties. Since these characteristics differ between species, it is obvious that the WF attributes have been used for classification (Reitberger et al. 2008; Alexander et al. 2010; Heinzel and Koch 2011; Mallet et al. 2011). The interpretation of WF data is not always straightforward. The bulk of the literature uses Gaussian WF decomposition, because software tools are available for the task (Roncat et al. 2014b). Other functions can also be fitted to the WF (Mallet et al. 2010; Roncat et al. 2014a). In vegetation, the WF is always a sum of the signals from several distinct scatterers that overlap due to their convolution with the emitted pulse. In this thesis I have used a simple algorithm to extract attributes directly from recorded WF sequences. The first noise-exceeding interaction of sufficient duration was treated as an entity for which the attributes were calculated. My approach is computationally efficient and remains independent of the assumptions about the shape of the system WF. However, the features are dependent on the sensor settings applied. The use of the first interaction is justified because transmission losses start there and subsequently weaken all further interactions.

Study III evaluated the potential of WF LiDAR in characterizing small trees and short-stature vegetation types. Some studies have been published that utilize DR LiDAR of approximately the same pulse density in a similar environment (Næsset and Bjerknes 2001; Korpela et al. 2008; Korhonen et al. 2013a), and some of these studies utilized passive optical data in combination with LiDAR. In addition, there are studies with very high density LiDAR (e.g., paper IV in Nyström 2014), but to my knowledge there are very few studies that have used WF LiDAR. As previously mentioned, WF data was able to capture the footprint-scale characteristics of vegetation structure (echo width, energy to amplitude ratio) and also reflectance properties (energy). In Finnish silviculture, the characterization of seedling and sapling stand vegetation is important for determining the pre-commercial treatments of young forests (Korpela et al. 2008; Korhonen et al. 2013a). The results of study III are also more widely applicable and indicate the general potential of WF data in the classification of low vegetation types (Vierling et al. 2012). Both simulated and real data implicated the importance of using large enough footprints (over 0.3–0.36 m in diameter) to achieve optimal classification. Incorporating the developed features into an imputation scheme that may be used to predict treatment needs constitutes a topic worthy of further study. At the same time, attention should also be paid to the use of WF data for improving the quality of digital elevation models (Wagner et al. 2008) that is important in low vegetation LiDAR RS. The predictions for species of small trees, particularly the separability of spruce from broadleaved species, were not as promising as in the four vegetation functional groups. Treatment needs should therefore perhaps be interpreted directly from LiDAR predictor features, without first predicting the species composition or other stand attributes. On the other hand, treatment needs are not always assessed unambiguously even in the field (Korhonen et al. 2013a), which poses challenges for developing RS solutions.

Study IV investigated the effects of tree species, phenology, height, site type, scan zenith angle, non-quantified (or 'difficult-to-quantify') structural differences between trees (the ‘tree effect’), and pulse density on the statistical tree-level WF features which were means of the WF attributes. The three main species in Finland differed clearly in WF attributes. Study IV provided explanations for these differences and validated the classification results against well-performing DR intensity features, previously presented in Korpela et al. (2010b). The results confirmed the potential of WF data for species classification that had already been shown in various temperate and boreal tree populations (Reitberger et al. 2008; Heinzel and Koch 2011; Vaughn et al. 2012; Lindberg et al. 2014; Yu et al. 2014). The effects of other canopy characteristics or thorough feature analyses have often been omitted in tree species classification studies. Thus, the quantification of the 'other than species' effects was an important contribution in study IV. It was shown that the majority of the feature variance comes from the tree effect. This inherent source of variation explains why perfect classification accuracy remains unattainable, although the correlation structures of different effects were not investigated. Several other findings were made, of which the influence of tree size and phenological status on WF attributes were most important. The study was limited to one sensor type with a 1064 nm wavelength and a relatively long (7–10 ns) system WF. According to the simulations in study III, the WF attributes in the simulated species were not particularly sensitive to sensor parameters other than the footprint size.

To summarize, species predictions using WF data were performed in studies III and IV. The results were more promising in large rather than small trees, which may be explained by age-related trends in tree structure. The WF data provided additional information compared to sole use of DR intensity metrics. The possibility to calculate the total energy from the WF was the most important factor contributing to performance improvement. This is in accordance with other studies that refer to the energy as 'intensity' or backscatter cross-section, in the case of calibrated data (Reitberger et al. 2008; Alexander 2010; Wagner 2010). Based on the LME modeling results, the energy in only-return data is least prone to variations in pulse density. The initial results of recent experiments (unpublished) suggest that the classification performance for individual trees is not significantly reduced when the pulse density decreases down to 2 per m^2, if energy is included in the set of predictors.

4.4 Outlook for future method and sensor development

Based on the outcomes of the thesis, I see two main research directions that can improve the utility of airborne LiDAR measurements, and our current understanding. Firstly, the data from new advanced WF-recording and multispectral LiDAR sensors should be put to use. Secondly, our understanding of the measurement process should be incorporated into a physical modeling environment, which is continuously updated as knowledge on LiDAR measurement and the geometric-optical properties of vegetation accumulates.

The use of WF features for species classification may remain somewhat limited in practice if they cannot be radiometrically calibrated to make them comparable between acquisitions, especially if the sensor(s) cannot be set to operate under exactly similar settings when a campaign takes place over a longer period of time. Relatively little is known about the stability of the emitted power of the sensors, and this poses an initial question to be investigated. A second concerns the stability of atmospheric conditions. If the emitted power and atmosphere do not vary significantly, then it would be sufficient to acquire data using similar sensor settings. If there is significant variation however, then vicarious calibration with reference surfaces is needed. In that case, the calibration results are dependent on how accurately the reflectance of the calibration targets can be determined (Kaasalainen et al. 2009). In theory, the calibration (vicarious or absolute) would also enable observations to be brought into same scale, independent of the flying altitude or footprint size. However, calibration may be ill-posed in vegetation that comprise complex scatterers that are neither point-like nor area-extended, and the footprint size may thus exercise an effect. Empirical evidence for the effects of footprint-target geometry is scarce (Korpela et al. 2010a; Gatziolis 2011). The effect of footprint size should be studied in a controlled environment (using the same sensor, and acquisitions on the same day under similar conditions, with stable calibration targets) so that any confusing effects can be excluded. Another important aspect is the phenology of vegetation that was seen to affect the signals in tree crowns. Repeated flights during the growing season could reveal more about the magnitude of these phenological effects and about the optimal time period for acquisitions. Tests with footprint and phenology would indicate how much variation may be allowed in the sensor parameters and in the time of acquisition without compromising the classification results.

Any new data should be applicable to serve operational systems such as the forest inventory methods of forest management planning which are area-based in Finland, Sweden, and Norway (Maltamo and Packalén 2014; Næsset 2014). Besides calibration, there are some other practical problems regarding the application of WF features for the estimation of tree species. One of the problems is the storage frequency of WFs which in many sensors is currently limited below the PRF because of deficits in data transfer capacity. The results of this thesis and other studies (e.g. Yu et al. 2014), which apply to single tree estimation, suggest that WF features may work reasonably well in low pulse density data, but further research is needed to confirm these results, especially in the context of area-based estimation of forest variables by species. In the area-based system, individual trees cannot normally be georeferenced in the field due to the high costs of field work. Species predictions could possibly be undertaken at individual tree or tree group level, using pure one-species plots as training data (Packalén et al. 2009). On the other hand, performing LiDAR-based predictions for single-tree remote sensing (Korpela 2004; Vauhkonen et al. 2010) utilizing high pulse density forms a separate research direction. More detailed description about the within-crown variation of radiometric data (as shown for vertical trends in Korpela et al. 2010b), and also in WF attributes, could result in even more accurate species identification results compared to those reported here.

Considering sensor development, the use of multiple wavelengths is the most obvious direction of development. Multiple wavelengths could potentially be used for improving species classification, but also for a more accurate quantification of the photosynthetically active biomass because the relative order of reflectance between foliage and bark differs between wavelengths (Morsdorf et al. 2009; Danson et al. 2014). This latter idea remains rather speculative as airborne LiDAR pulses do normally not penetrate to the internal parts of the tree crown (Figure 6). On the other hand, using multiple footprints (a 'multi-divergent sensor') could characterize the gap-size distribution in the canopy, which may hold species-specific traits.

Considering the utilization of WF data to their full potential, this thesis has analyzed only those WF attributes extracted for each 'first echo' or NEAS. Using the aggregate vertical distribution of energy from multiple WFs at the tree crown or plot level is another option. Unlike DR echo height distributions or the WF attributes, the vertical energy distribution should be rather invariant to issues such as footprint size, although it could be slightly ‘reduced at the tails’ when the footprint size increases due to the reduced SNR (Hopkinson 2007). Vertical energy distribution, particularly if corrected for transmission losses, has been shown to improve the characterization of forest vertical structure (vertical profiles of crown volume over many trees), compared to DR echo data (Lindberg et al. 2012). However, the gain from using WF data may depend on the maximum number of DR echoes extracted per pulse. A potential application of vertical energy distributions is the detection of understory trees as discussed in Section 4.1. In individual trees, the crown length is related to stem diameter (Korhonen et al. 2013b) and stem form (Jonson 1912) - the corollary being that crown length is linked with stem volume. All of the parameters mentioned above are important for estimating the assortment of merchantable timber through stem tapering (cf. Laasasenaho 1982).

Many questions related to the use of LiDAR data in forest inventories could potentially be solved using a modeling environment that can reliably simulate LiDAR data with arbitrary sensor or acquisition configurations. More basic research is required to acquire data for input parameters, and also to validate models. Firstly, more laboratory measurements must be conducted in order to perfectly understand the optical properties of elementary scattering objects (such as leaves or needles) in coherent light and in the backscatter geometry (Kaasalainen and Rautiainen 2007). Secondly, measurements of individual shoots or branches in laboratory conditions (Mõttus et al. 2012) should be compared with simulations, and the sensitivity of simulation results should be tested against variations in low-level (leaf, shoot, branch) parameters. Thirdly, measurement with TLS (Pfeifer et al. 2004; Côté et al. 2009; Raumonen et al. 2013) should be utilized to generate a library of model trees or forest plots that, when coupled with measured optical properties, should prove realistic and representative enough to serve as a virtual test field that can be used to challenge various hypotheses related to the interpretation of LiDAR data and the development of sensors. Finally, a better understanding of the functioning of LiDAR receivers is needed, particularly considering the various components of noise and the receiver response function. Ideally, sensors should be perfectly linear and stable in their response, and exercise low variation in the characteristics of the emitted pulse, which would facilitate radiometrically quantitative LiDAR remote sensing and enable comparisons of simulated and real data.

I see the most obvious applications of the simulation models in the testing of sensors and hypotheses that are then later complemented and verified with field experiments. A more ambitious approach would be to attempt model inversion in order to derive forest variables from the simulated data. Direct inversion is not possible for MCRT, but one might perhaps use a look-up-table approach (e.g., Knyazikhin et al. 1998) to achieve this aim. Certainly however, any geometric-optical models used would need to capture the natural variation in vegetation in order to be practically applicable. In addition, the 'uncertain allometric step backwards' from the properties of the scatterers to the desired forest variables (e.g. stem volume) remains a challenge. In other words, we may be able to physically simulate the relation between the geometric-optical properties of vegetation and the LiDAR signal, but we still need a statistical or physiological model to understand the relationship between the geometric-optical properties and the forest variables of interest (cf. Figure 4). Other potential examples of the use of models are the estimation of forest growth from multi-temporal LiDAR data, or the prediction of different above-ground forest biomass components. Field data for growth or biomass are difficult to obtain, but both provide relevant topics from an application perspective. Finally, one should not overlook the knowledge and understanding that accumulates during such model development, even if direct applications may not always seem obvious.

Because of the basic nature of research conducted in this thesis, the discussion of other RS methods was purposefully omitted. However, relevant LiDAR research will always be driven by applications. For example, it has been speculated that the next generation implementation of forest management planning inventories in Finland could be entirely based on the passive imagery as the RS data source. Because of its direct 3D nature, LiDAR provides fundamental benefits for vegetation mapping, and I believe that it will remain a relevant option in forestry applications for many years. Therefore, there is still lots of room for basic research on the complex interplay between LiDAR pulses, vegetation and sensors. Such research will hopefully reveal new ways of interpreting measurements and developing sensors, which may then in turn contribute to the efficient and rational use of forest resources.

REFERENCES

Ahokas E., Kaasalainen S., Hyyppä J., Suomalainen J. (2006). Calibration of the Optech ALTM 3100 laser scanner intensity data using brightness targets. International Archives of the Photogrammetry, Remote Sensing and Spatial Information Sciences XXXVI part 1: 1–6.

Ahokas E., Hyyppä J., Yu X., Holopainen M. (2011). Transmittance of airborne laser scanning pulses for boreal forest elevation modeling. Remote Sensing 3: 1365–1379. http://dx.doi.org/10.3390/rs3071365

Alexander C., Tansey K., Kaduk J., Holland D., Tate N.J. (2010). Backscatter coefficient as an attribute for the classification of full-waveform airborne laser scanning data in urban areas. ISPRS Journal of Photogrammetry and Remote Sensing 65: 423–432. http://dx.doi.org/10.1016/j.isprsjprs.2010.05.002

Baltsavias E.P. (1999a). Airborne laser scanning: Basic relations and formulas. ISPRS Journal of Photogrammetry and Remote Sensing 54: 199–214. http://dx.doi.org/10.1016/S0924-2716(99)00015-5

Beisl U. (2006). Absolute spectroradiometric calibration of the ADS40 sensor. International Archives of the Photogrammetry, Remote Sensing and Spatial Information Sciences XXXVI part 1. 5 p.

Bousquet L., Lacherade S., Jacquemoud S., Moya I. (2005). Leaf BRDF measurements and model for specular and diffuse components differentiation. Remote Sensing of Environment 98: 201–211. http://dx.doi.org/10.1016/j.rse.2005.07.005

Breidenbach J., Næsset E., Lien V., Gobakken T., Solberg S. (2010). Prediction of species specific forest inventory attributes using a nonparametric semi-individual tree crown approach based on fused airborne laser scanning and multispectral data. Remote Sensing of Environment 114: 911–924. http://dx.doi.org/10.1016/j.rse.2009.12.004

Calders K., Lewis P., Disney M., Verbesselt J. Herold M. (2013). Investigating assumptions of crown archetypes for modelling LiDAR returns. Remote Sensing of Environment 134: 39–49. http://dx.doi.org/10.1016/j.rse.2013.02.018

Chandrasekhar S. (1950). Radiative transfer. Dover publications, New York, USA. 393 p.

Chasmer L., Hopkinson C., Smith B., Treitz P. (2006). Examining the influence of changing laser pulse repetition frequencies on conifer forest canopy returns. Photogrammetric Engineering and Remote Sensing 72: 1359–1367. http://dx.doi.org/10.14358/PERS.72.12.1359

Chauve A., Vega C., Durrieu S., Bretar F., Allouis T., Deseilligny M.P., Puech W. (2009). Advanced full-waveform lidar data echo detection: Assessing quality of derived terrain and tree height models in an alpine coniferous forest. International Journal of Remote Sensing 30: 5211–5228. http://dx.doi.org/10.1080/01431160903023009

Côté J-F., Widlowski J-L., Fournier R.A., Verstraete M.M. (2009). The structural and radiative consistency of three-dimensional tree reconstructions from terrestrial lidar. Remote Sensing of Environment 113: 1067–1081. http://dx.doi.org/10.1016/j.rse.2009.01.017

Danson F.M., Gaulton R., Armitage R.P., Disney M., Gunawan O., Lewis P., Pearson G., Ramirez A.F. (2014). Developing a dual-wavelength full-waveform terrestrial laser scanner to characterize forest canopy structure. Agricultural and Forest Meteorology 198: 7–14. http://dx.doi.org/10.1016/j.agrformet.2014.07.007

de Wit C.T. (1965). Photosynthesis of leaf canopies. Agricultural Research Reports 663, Institute for Biological and Chemical Research on Field Crops and Herbage, Wageningen, The Netherlands. 57 p.

Disney M.I., Lewis P., North P.R.J. (2000). Monte Carlo ray tracing in optical canopy reflectance modelling. Remote Sensing Reviews 18: 163–196. http://dx.doi.org/10.1080/02757250009532389

Disney M., Lewis P., Saich P. (2006). 3D modelling of forest canopy structure for remote sensing simulations in the optical and microwave domains. Remote Sensing of Environment 100: 114–132. http://dx.doi.org/10.1016/j.rse.2005.10.003

Disney M.I., Kalogirou V., Lewis P., Prieto-Blanco A., Hancock S. Pfeifer M. (2010). Simulating the impact of discrete-return lidar system and survey characteristics over young conifer and broadleaf forests. Remote Sensing of Environment 114: 1546–1560. http://dx.doi.org/10.1016/j.rse.2010.02.009

Doneus M., Briese C., Studnicka N. (2010). Analysis of full-waveform ALS data by simultaneously acquired TLS data: Towards an advanced DTM generation in wooded areas. International Archives of the Photogrammetry, Remote Sensing and Spatial Information Sciences XXXVII part 7B: 193–198.

Gatziolis D. (2011). Dynamic range-based intensity normalization for airborne, discrete return lidar data of forest canopies. Photogrammetric Engineering and Remote Sensing 77: 251–259. http://dx.doi.org/10.14358/PERS.77.3.251

Gobakken T., Næsset E. (2008). Assessing effects of laser point density, ground sampling intensity, and field sample plot size on biophysical stand properties derived from airborne laser scanner data. Canadian Journal of Forest Research 38: 1095–1109. http://dx.doi.org/10.1139/X07-219

Goodman J.W. (1976). Some fundamental properties of speckle. Journal of the Optical Society of America 66: 1145–1150. http://dx.doi.org/10.1364/JOSA.66.001145

Habib A., Bang K.I., Kersting A.P., Lee D. (2009). Error budget of lidar systems and quality control of the derived data. Photogrammetric Engineering and Remote Sensing 75: 1093–1108. http://dx.doi.org/10.14358/PERS.75.9.1093

Hapke B., DiMucci D., Nelson R., Smythe W. (1996). The cause of the hot spot in vegetation canopies and soils: Shadow-hiding versus coherent backscatter. Remote Sensing of Environment 58: 63–68. http://dx.doi.org/10.1016/0034-4257(95)00257-X

Harding D.J., Carabajal C.C. (2005). ICESat waveform measurements of within-footprint topographic relief and vegetation vertical structure. Geophysical Research Letters 32: L21–S10. http://dx.doi.org/10.1029/2005GL023471

Heinzel J., Koch B. (2011). Exploring full-waveform LiDAR parameters for tree species classification. International Journal of Applied Earth Observation and Geoinformation 13: 152–160. http://dx.doi.org/10.1016/j.jag.2010.09.010

Hill R.A., Broughton R.K. (2009). Mapping the understorey of deciduous woodland from leaf-on and leaf-off airborne LiDAR data: A case study in lowland britain. ISPRS Journal of Photogrammetry and Remote Sensing 64: 223–233. http://dx.doi.org/10.1016/j.isprsjprs.2008.12.004

Höfle, B. Pfeifer, N. (2007). Correction of laser scanning intensity data: Data and model-driven approaches. ISPRS Journal of Photogrammetry and Remote Sensing 62: 415–433. http://dx.doi.org/10.1016/j.isprsjprs.2007.05.008

Hofton M.A., Minster J.B., Blair J.B. (2000). Decomposition of laser altimeter waveforms. IEEE Transactions on Geoscience and Remote Sensing 38: 1989–1996. http://dx.doi.org/10.1109/36.851780

Hollaus M., Mücke W., Höfle B., Dorigo W., Pfeifer N., Wagner W., Bauerhansl C., Regner B. (2009). Tree species classification based on full-waveform airborne laser scanning data. Proceedings of Silvilaser 2009, October 14–16, College Station, Texas, USA. 9 p.

Hollaus M., Mücke W., Roncat A., Pfeifer N., Briese C. (2014). Full-waveform airborne laser scanning systems and their possibilities in forest applications. In: Maltamo M., Næsset E., Vauhkonen J. (eds.). Forestry applications of airborne laser scanning - Concepts and case studies. Managing Forest Ecosystems 27, Springer, The Netherlands, p. 43–61. http://dx.doi.org/10.1007/978-94-017-8663-8_3

Holmgren J., Nilsson M., Olsson H. (2003). Simulating the effects of lidar scanning angle for estimation of mean tree height and canopy closure. Canadian Journal of Remote Sensing 29: 623−632. http://dx.doi.org/10.5589/m03-030

Holmgren J., Persson Å. (2004). Identifying species of individual trees using airborne laser scanner. Remote Sensing of Environment 90: 415–423. http://dx.doi.org/10.1016/S0034-4257(03)00140-8

Hopkinson C. (2007). The influence of flying altitude, beam divergence, and pulse repetition frequency on laser pulse return intensity and canopy frequency distribution. Canadian Journal of Remote Sensing 33: 312–324. http://dx.doi.org/10.5589/m07-029

Hopkinson C., Chasmer L. (2009). Testing LiDAR models of fractional cover across multiple forest ecozones. Remote Sensing of Environment 113: 275–288. http://dx.doi.org/10.1016/j.rse.2008.09.012

Hosgood B., Jacquemoud S., Andreoli G., Verdebout J., Pedrini A., Schmuck G. (2005). Leaf Optical Properties EXperiment 93 (LOPEX93). Report EUR 16095 EN (revised 2005), European Commission, Joint Research Centre, Institute for Remote Sensing Applications, ISPRA, Italy. 7 p.

Hyyppä J., Hyyppä H., Leckie D., Gougeon F., Yu X., Maltamo M. (2008). Review of methods of small-footprint airborne laser scanning for extracting forest inventory data in boreal forests. International Journal of Remote Sensing 29: 1339–1366. http://dx.doi.org/10.1080/01431160701736489

Hyyppä J., Inkinen M. (1999). Detecting and estimating attributes for single trees using laser scanner. Photogrammetric Journal of Finland 16: 27–42.

Jalobeanu A., Gonçalves G.R. (2012). The full-waveform LiDAR Riegl LMS-Q680i: from reverse engineering to sensor modeling. In: ASPRS Annual Conference 2012, Sacramento, CA, USA. 9 p.

Jaskierniak D., Lane P.N.J., Robinson A., Lucieer A. (2011). Extracting LiDAR indices to characterise multilayered forest structure using mixture distribution functions. Remote Sensing of Environment 115: 573–585. http://dx.doi.org/10.1016/j.rse.2010.10.003

Jelalian A.V. (1992). Laser Radar Systems. Artech House, Boston, London. 308 p.

Jonson T. (1912). Taxatoriska undersökningar öfver skogsträdens form. Skogsvårdsföreningens tidskrift h. 4: 235–275.

Junninen H., Lauri A,. Keronen P., Aalto P., Hiltunen V., Hari P., Kulmala M. (2009). Smart-SMEAR: on-line data exploration and visualization tool for SMEAR stations. Boreal Environmental Research 14: 447−457.

Jutzi B., Stilla U. (2006a). Range determination with waveform recording laser systems using a wiener filter. ISPRS Journal of Photogrammetry and Remote Sensing 61: 95–107. http://dx.doi.org/10.1016/j.isprsjprs.2006.09.001

Jutzi B., Stilla U. (2006b). Characteristics of the measurement unit of a full-waveform laser system. International Archives of the Photogrammetry, Remote Sensing and Spatial Information Sciences XXXVI part 1A. 6 p.

Kaasalainen S., Ahokas E., Hyyppä J., Suomalainen J. (2005). Study of surface brightness from backscattered laser intensity: Calibration of laser data. IEEE Geoscience and Remote Sensing Letters 2: 255–259. http://dx.doi.org/10.1109/LGRS.2005.850534

Kaasalainen S., Hyyppä H., Kukko A., Litkey P., Ahokas E., Hyyppä J., Lehner H., Jaakkola A., Suomalainen J., Akujärvi A., Kaasalainen M., Pyysalo U. (2009). Radiometric calibration of LIDAR intensity with commercially available reference targets. IEEE Transactions on Geoscience and Remote Sensing 47: 588–598. http://dx.doi.org/10.1109/TGRS.2008.2003351

Kaasalainen S., Rautiainen M. (2007). Backscattering measurements from individual Scots pine needles. Applied Optics 46: 4916–4922. http://dx.doi.org/10.1364/AO.46.004916

Knyazikhin Y., Marshak A. (1991). Fundamental equations of radiative transfer in leaf canopies, and iterative methods for their solution. In: Myneni R.B., Ross J. (eds.). Photon-vegetation interactions - Applications in optical remote sensing and plant ecology. Springer-Verlag Berlin Heidelberg, Germany. p. 9–43. http://dx.doi.org/10.1007/978-3-642-75389-3_2

Knyazikhin Y., Martonchik J.V., Myneni R.B., Diner D.J., Running S.W. (1998). Synergistic algorithm for estimating vegetation canopy leaf area index and fraction of absorbed photosynthetically active radiation from MODIS and MISR data. Journal of Geophysical Research 103: 32257–32275. http://dx.doi.org/10.1029/98JD02462

Korhonen L., Korpela I., Heiskanen J., Maltamo M. (2011). Airborne discrete-return LiDAR data in the estimation of vertical canopy cover, angular canopy closure and leaf area index. Remote Sensing of Environment 115: 1065–1080. http://dx.doi.org/10.1016/j.rse.2010.12.011

Korhonen L., Pippuri I., Packalén P., Heikkinen V., Maltamo M., Heikkilä J. (2013a). Detection of the need for seedling stand tending using high-resolution remote sensing data. Silva Fennica 47: article id 952, 20 p. http://dx.doi.org/10.14214/sf.952

Korhonen L., Vauhkonen J., Virolainen A., Hovi A., Korpela I. (2013b). Estimation of tree crown volume from airborne lidar data using computational geometry. International Journal of Remote Sensing 34: 7236–7248. http://dx.doi.org/10.1080/01431161.2013.817715

Korpela I. (2004). Individual tree measurements by means of digital aerial photogrammetry. Silva Fennica - Monographs 3. 93 p.

Korpela I. (2006). Geometrically accurate time series of archived aerial images and airborne lidar data in a forest environment. Silva Fennica 40: 109–126. http://dx.doi.org/10.14214/sf.355

Korpela I.S. (2008). Mapping of understory lichens with airborne discrete-return LiDAR data. Remote Sensing of Environment 112: 3891–3897. http://dx.doi.org/10.1016/j.rse.2008.06.007

Korpela I., Tuomola T., Tokola T., Dahlin B. (2008). Appraisal of seedling stand vegetation with airborne imagery and discrete-return LiDAR - an exploratory analysis. Silva Fennica 42: 753–772. http://dx.doi.org/10.14214/sf.466

Korpela I. , Tuomola T., Välimäki E. (2007). Mapping forest plots: An efficient method combining photogrammetry and field triangulation. Silva Fennica 41: 457−469. http://dx.doi.org/10.14214/sf.283

Korpela I., Ørka H.O., Hyyppä J., Heikkinen V., Tokola T. (2010a). Range and AGC normalization in airborne discrete-return LiDAR intensity data for forest canopies. ISPRS Journal of Photogrammetry and Remote Sensing 65: 369–379. http://dx.doi.org/10.1016/j.isprsjprs.2010.04.003

Korpela I., Ørka H.O., Maltamo M., Tokola T., Hyyppä J. (2010b). Tree species classification using airborne LiDAR - effects of stand and tree parameters, downsizing of training set, intensity normalization, and sensor type. Silva Fennica 44: 319–339. http://dx.doi.org/10.14214/sf.156

Kotchenova S.Y., Shabanov N.V., Knyazikhin Y., Davis A.B., Dubayah R., Myneni R.B. (2003). Modeling lidar waveforms with time-dependent stochastic radiative transfer theory for remote estimations of forest structure. Journal of Geophysical Research-Atmospheres 108(D15): 4484. http://dx.doi.org/10.1029/2002JD003288

Kuusk A. (1991). The hot-spot effect in plant canopy reflectance. In: Myneni R.B., Ross J. (eds.). Photon-vegetation interactions - applications in optical remote sensing and plant ecology. Springer-Verlag Berlin Heidelberg, Germany. p. 139–158. http://dx.doi.org/10.1007/978-3-642-75389-3_5

Kuusk A., Lang M., Nilson T. (2004). Simulation of the reflectance of ground vegetation in sub-boreal forests. Agricultural and Forest Meteorology 126: 33–46. http://dx.doi.org/10.1016/j.agrformet.2004.05.004

Laasasenaho J. (1982). Taper curve and volume functions for pine, spruce and birch. Communicationes Instituti Forestalis Fenniae 108: 1–74.

Lang M., Kuusk A., Nilson T., Lükk T., Pehk M., Alm G. (2002). Reflectance spectra of ground vegetation in sub-boreal forests. Web page. Available online from Tartu Observatory, Estonia. http://www.aai.ee/bgf/ger2600/. [Cited 6 Feb 2013].

Lefsky M.A., Harding D., Cohen W.B., Parker G., Shugart H.H. (1999). Surface lidar remote sensing of basal area and biomass in deciduous forests of eastern Maryland, USA. Remote Sensing of Environment 67: 83–98. http://dx.doi.org/10.1016/S0034-4257(98)00071-6

Leica (2015). Leica Geosystems AG company web pages. http://www.leica-geosystems.com. [Cited 19 Feb 2015].

Leiterer R., Mücke W., Morsdorf F., Hollaus M., Pfeifer N., Schaepman M.E. (2013). Operational forest structure monitoring using airborne laser scanning. Photogrammetrie-Fernerkundung-Geoinformation 2013.3: 173–184. http://dx.doi.org/10.1127/1432-8364/2013/0168

Li J., Hu B. Noland T.L. (2013). Classification of tree species based on structural features derived from high density LiDAR data. Agricultural and Forest Meteorology 171: 104–114. http://dx.doi.org/10.1016/j.agrformet.2012.11.012

Lim K., Treitz P., Wulder M., St-Onge B., Flood M. (2003). LiDAR remote sensing of forest structure. Progress in Physical Geography 27: 88–106. http://dx.doi.org/10.1191/0309133303pp360ra

Lindberg E., Eysn L., Hollaus M., Holmgren J., Pfeifer N. (2014). Delineation of tree crowns and tree species classification from full-waveform airborne laser scanning data using 3-D ellipsoidal clustering. IEEE Journal of Selected Topics in Applied Earth Observations and Remote Sensing 7: 3174–3181. http://dx.doi.org/10.1109/JSTARS.2014.2331276

Lindberg E., Olofsson K., Holmgren J., Olsson H. (2012). Estimation of 3D vegetation structure from waveform and discrete return airborne laser scanning data. Remote Sensing of Environment 118: 151–161. http://dx.doi.org/10.1016/j.rse.2011.11.015

Lintunen A., Sievänen R., Kaitaniemi P., Perttunen J. (2011). Models of 3D crown structure for Scots pine (*Pinus sylvestris*) and silver birch (*Betula pendula*) grown in mixed forest. Canadian Journal of Forest Research 41: 1779–1794. http://dx.doi.org/10.1139/x11-092

Lukeš P., Stenberg P., Rautiainen M., Mõttus M., Vanhatalo K.M. (2013). Optical properties of leaves and needles for boreal tree species in Europe. Remote Sensing Letters 4: 667–676. http://dx.doi.org/10.1080/2150704X.2013.782112

Magnussen S., Boudewyn P. (1998). Derivations of stand heights from airborne laser scanner data with canopy-based quantile estimators. Canadian Journal of Forest Research 28: 1016–1031. http://dx.doi.org/10.1139/x98-078

Mallet C., Bretar F. (2009). Full-waveform topographic lidar: State-of-the-art. ISPRS Journal of Photogrammetry and Remote Sensing 64: 1–16. http://dx.doi.org/10.1016/j.isprsjprs.2008.09.007

Mallet C., Bretar F., Roux M., Sörgel U., Heipke C. (2011). Relevance assessment of full-waveform lidar data for urban area classification. ISPRS Journal of Photogrammetry and Remote Sensing 66: S71–S84. http://dx.doi.org/10.1016/j.isprsjprs.2011.09.008

Mallet C., Lafarge F., Roux M., Sörgel U., Bretar F., Heipke C. (2010). A marked point process for modeling lidar waveforms. IEEE Transactions on Image Processing 19: 3204–3221. http://dx.doi.org/10.1109/TIP.2010.2052825

Maltamo M., Packalén P. (2014). Species-specific management inventory in Finland. In: Maltamo M., Næsset E., Vauhkonen J. (eds.). Forestry applications of airborne laser scanning: Concepts and case studies. Managing Forest Ecosystems 27, Springer, The Netherlands, p. 241–252. http://dx.doi.org/10.1007/978-94-017-8663-8_12

Maltamo M., Packalén P., Yu X., Eerikäinen K., Hyyppä J., Pitkänen J. (2005). Identifying and quantifying structural characteristics of heterogeneous boreal forests using laser scanner data. Forest Ecology and Management 216: 41–50. http://dx.doi.org/10.1016/j.foreco.2005.05.034

Martinuzzi S., Vierling L.A., Gould W.A., Falkowski M.J., Evans J.S., Hudak A.T., Vierling K.T. (2009). Mapping snags and understory shrubs for a LiDAR-based assessment of wildlife habitat suitability. Remote Sensing of Environment 113: 2533–2546. http://dx.doi.org/10.1016/j.rse.2009.07.002

Means J.E., Acker S.A., Harding D.J., Blair J.B., Lefsky M.A., Cohen W.B., Harmone M.E., McKee W.A. (1999). Use of large-footprint scanning airborne lidar to estimate forest stand characteristics in the western cascades of Oregon. Remote Sensing of Environment 67: 298–308. http://dx.doi.org/10.1016/S0034-4257(98)00091-1

McCulloch C.E., Searle S.R., Neuhaus J.M. (2008). Generalized, linear, and mixed models. John Wiley & Sons, Hoboken, New Jersey, USA, 2nd ed. 424 p.

Morsdorf F., Marell A., Koetz B., Cassagne N., Pimont F., Rigolot E., Allgöwer B. (2010). Discrimination of vegetation strata in a multi-layered mediterranean forest ecosystem using height and intensity information derived from airborne laser scanning. Remote Sensing of Environment 114: 1403–1415. http://dx.doi.org/10.1016/j.rse.2010.01.023

Morsdorf F., Nichol C., Malthus T. Woodhouse I.H. (2009). Assessing forest structural and physiological information content of multi-spectral LiDAR waveforms by radiative transfer modelling. Remote Sensing of Environment 113: 2152–2163. http://dx.doi.org/10.1016/j.rse.2009.05.019

Mõttus M., Rautiainen M., Schaepman M.E. (2012). Shoot scattering phase function for Scots pine and its effect on canopy reflectance. Agricultural and Forest Meteorology 154: 67–74. http://dx.doi.org/10.1016/j.agrformet.2011.10.012

Næsset E. (1997a). Determination of mean tree height of forest stands using airborne laser scanner data. ISPRS Journal of Photogrammetry and Remote Sensing 52: 49–56. http://dx.doi.org/10.1016/S0924-2716(97)83000-6

Næsset E. (1997b). Estimating timber volume of forest stands using airborne laser scanner data. Remote Sensing of Environment 61: 246–253. http://dx.doi.org/10.1016/S0034-4257(97)00041-2

Næsset E. (2002). Predicting forest stand characteristics with airborne scanning laser using a practical two-stage procedure and field data. Remote Sensing of Environment 80: 88–99. http://dx.doi.org/10.1016/S0034-4257(01)00290-5

Næsset E. (2009). Effects of different sensors, flying altitudes, and pulse repetition frequencies on forest canopy metrics and biophysical stand properties derived from small-footprint airborne laser data. Remote Sensing of Environment 113: 148–159. http://dx.doi.org/10.1016/j.rse.2008.09.001

Næsset E. Bjerknes K.O. (2001). Estimating tree heights and number of stems in young forest stands using airborne laser scanner data. Remote Sensing of Environment 78: 328–340. http://dx.doi.org/10.1016/S0034-4257(01)00228-0

Næsset E., Gobakken T. (2008). Estimation of above- and below-ground biomass across regions of the boreal forest zone using airborne laser. Remote Sensing of Environment 112: 3079–3090. http://dx.doi.org/10.1016/j.rse.2008.03.004

Næsset E., Gobakken T., Holmgren J., Hyyppä H., Hyyppä J., Maltamo M., Nilsson M., Olsson H., Persson Å., Söderman U. (2004). Laser scanning of forest resources: The Nordic experience. Scandinavian Journal of Forest Research 19: 482–499. http://dx.doi.org/10.1080/02827580410019553

Næsset E. (2014). Area-based Inventory in Norway – from innovation to an operational reality. In: Maltamo M., Næsset E., Vauhkonen J. (eds.). Forestry Applications of Airborne Laser Scanning: Concepts and Case Studies. Managing Forest Ecosystems 27, Springer, the Netherlands, p. 215–240. http://dx.doi.org/10.1007/978-94-017-8663-8_11

Nelson R. (2013). How did we get here? An early history of forestry lidar. Canadian Journal of Remote Sensing 39: S6–S17. http://dx.doi.org/10.5589/m13-011

Nilsson M. (1996). Estimation of tree heights and stand volume using an airborne lidar system. Remote Sensing of Environment 56: 1–7. http://dx.doi.org/10.1016/0034-4257(95)00224-3

Ni-Meister W., Jupp D.L.B. Dubayah R. (2001). Modeling lidar waveforms in heterogeneous and discrete canopies. IEEE Transactions on Geoscience and Remote Sensing 39: 1943–1958. http://dx.doi.org/10.1109/36.951085

North P.R.J., Rosette J.A.B., Suarez J.C., Los S.O. (2010). A Monte Carlo radiative transfer model of satellite waveform LiDAR. International Journal of Remote Sensing 31: 1343–1358. http://dx.doi.org/10.1080/01431160903380664

Nyström M. (2014). Mapping and monitoring of vegetation using airborne laser scanning. Doctoral thesis, Swedish University of Agricultural Sciences, Umeå, Sweden. 72 p.

Nyyssönen A. (1955). On the estimation of the growing stock from aerial photographs. Communicationes Instituti Forestalis Fenniae 46: 1–57.

Optech (2015). Optech Inc. company web pages. http://www.optech.com. [Cited 19 Feb 2015].

Ørka H.O., Næsset E., Bollandsås O.M. (2009). Classifying species of individual trees by intensity and structure features derived from airborne laser scanner data. Remote Sensing of Environment 113: 1163–1174. http://dx.doi.org/10.1016/j.rse.2009.02.002

Packalén P., Maltamo M. (2007). The k-MSN method for the prediction of species-specific stand attributes using airborne laser scanning and aerial photographs. Remote Sensing of Environment 109: 328–341. http://dx.doi.org/10.1016/j.rse.2007.01.005

Packalén P., Suvanto A., Maltamo M. (2009). A two stage method to estimate species-specific growing stock. Photogrammetric Engineering and Remote Sensing 75: 1451–1460. http://dx.doi.org/10.14358/PERS.75.12.1451

Persson Å., Holmgren J. Söderman U. (2002). Detecting and measuring individual trees using an airborne laser scanner. Photogrammetric Engineering and Remote Sensing 68: 925–932.

Petrie G., Toth C.K. (2009). Introduction to laser ranging, profiling and scanning. In: Shan J., Toth C.K. (eds.). Topographic laser ranging and scanning: Principles and processing. Taylor & Francis Group, Boca Raton, FL, USA. p. 1–27.

Pfeifer N., Gorte B., Winterhalter D. (2004). Automatic reconstruction of single trees from terrestrial laser scanner data. International Archives of the Photogrammetry, Remote Sensing and Spatial Information Sciences XXXV-B5: 114–119.

Pfenningbauer M., Ullirhch A. (2011). Multi-wavelength airborne laser scanning. International LiDAR mapping forum 2011, Feb 7–9, New Orleans, USA, 10 p.

Pisek J., Ryu Y., Alikas K. (2011). Estimating leaf inclination and G-function from leveled digital camera photography in broadleaf canopies. Trees-Structure and Function 25: 919–924. http://dx.doi.org/10.1007/s00468-011-0566-6

Poso S. (1983). Kuvioittaisen arvioimismenetelmän perusteita. English summary: Basic features of forest inventory by compartments. Silva Fennica 17: 313–349. http://dx.doi.org/10.14214/sf.a15179

Raumonen P., Kaasalainen M., Åkerblom M., Kaasalainen S., Kaartinen H., Vastaranta M., Holopainen M., Disney M., Lewis P. (2013). Fast automatic precision tree models from terrestrial laser scanner data. Remote Sensing 5: 491–520. http://dx.doi.org/10.3390/rs5020491

Reitberger J., Krzystek P., Stilla U. (2008). Analysis of full waveform LIDAR data for the classification of deciduous and coniferous trees. International Journal of Remote Sensing 29: 1407–1431. http://dx.doi.org/10.1080/01431160701736448

Richter K., Stelling N., Maas H.G. (2014). Correcting attenuation effects caused by interactions in the forest canopy in full-waveform ariborne laser scanner data. The International Archives of the Photogrammetry, Remote Sensing and Spatial Information Sciences XL-3: 273–280. http://dx.doi.org/10.5194/isprsarchives-XL-3-273-2014

Riegl (2015). Riegl GmbH company web pages. http://www.riegl.com. [Cited 19 Feb 2015].

Roncat A., Bergauer G., Pfeifer N. (2011). β-spline deconvolution for differential target cross-section determination in full-waveform laser scanning data. ISPRS Journal of Photogrammetry and Remote Sensing 66: 418-428. http://dx.doi.org/10.1016/j.isprsjprs.2011.02.002

Roncat A., Briese C., Jansa J., Pfeifer N. (2014a). Radiometrically calibrated features of full-waveform lidar point clouds based on statistical moments. IEEE Geoscience and Remote Sensing Letters 11: 549–553. http://dx.doi.org/10.1109/LGRS.2013.2274557

Roncat A., Morsdorf F., Briese C., Wagner W., Pfeifer N. (2014b). Laser pulse interaction with forest canopy: Geometric and radiometric issues. In: Maltamo M., Næsset E., Vauhkonen J. (eds.). Forestry applications of airborne laser scanning: Concepts and case studies. Managing Forest Ecosystems 27, Springer, The Netherlands. p. 19–41. http://dx.doi.org/10.1007/978-94-017-8663-8_2

Roth R. (2011). Leica ALS70 – point density multiplication for high density surface acquisition. In: Fritsch, D. (ed.). Photogrammetric Week 2011. p. 249–255.

Schaepman-Strub G., Schaepman M.E., Painter T.H., Dangel S., Martonchik J.V. (2006). Reflectance quantities in optical remote sensing-definitions and case studies. Remote Sensing of Environment 103: 27–42. http://dx.doi.org/10.1016/j.rse.2006.03.002

Smolander S., Stenberg P. (2003). A method to account for shoot scale clumping in coniferous canopy reflectance models. Remote Sensing of Environment 88: 363–373. http://dx.doi.org/10.1016/j.rse.2003.06.003

Solberg S., Brunner A., Hanssen K.H., Lange H., Næsset E., Rautiainen M., Stenberg P. (2009). Mapping LAI in a Norway spruce forest using laser scanning. Remote Sensing of Environment 113: 2317–2327. http://dx.doi.org/10.1016/j.rse.2009.06.010

Sun G.Q., Ranson K.J. (2000). Modeling lidar returns from forest canopies. IEEE Transactions on Geoscience and Remote Sensing 38: 2617–2626. http://dx.doi.org/10.1109/36.885208

Stilla U., Jutzi B. (2009). Waveform analysis for small-footprint pulsed laser systems. In: Shan J., Toth C.K. (eds.). Topographic laser ranging and scanning: Principles and processing. Taylor & Francis Group, Boca Raton, FL, USA. p. 215–234.

Suomalainen J., Hakala T., Peltoniemi J., Puttonen E. (2009). Polarised multiangular reflectance measurements using the Finnish geodetic institute field goniospectrometer. Sensors 9: 3891–3907. http://dx.doi.org/10.3390/s90503891

Talts J. (1977). Mätning i storskaliga flygbilder för beståndsdatainsamling. Summary: Photogrammetric measurements for stand cruising. Royal College of Forestry. Department of Forest Mensuration and Management. Research notes NR 6 – 1977. 102 p. [In Swedish]

Toth C.K. (2009). Strip adjustment and registration. In: Shan J., Toth C.K. (eds.). Topographic laser ranging and scanning: Principles and processing. Taylor & Francis Group, Boca Raton, FL, USA. p. 235–268.

Ullrich A., Pfenningbauer M. (2011). Echo digitization and waveform analysis in airborne and terrestrial laser scanning. In: Fritsch, D. (ed.). Photogrammetric Week 2011, 5–9 September, Stuttgart, Germany. p. 217–228.

Wagner W. (2010). Radiometric calibration of small-footprint full-waveform airborne laser scanner measurements: Basic physical concepts. ISPRS Journal of Photogrammetry and Remote Sensing 65: 505–513. http://dx.doi.org/10.1016/j.isprsjprs.2010.06.007

Wagner W., Hollaus M., Briese C., Ducic V. (2008). 3D vegetation mapping using small-footprint full-waveform airborne laser scanners. International Journal of Remote Sensing 29: 1433–1452. http://dx.doi.org/10.1080/01431160701736398

Wagner W., Ullrich A., Ducic V., Melzer T., Studnicka N. (2006). Gaussian decomposition and calibration of a novel small-footprint full-waveform digitising airborne laser scanner. ISPRS Journal of Photogrammetry and Remote Sensing 60: 100–112. http://dx.doi.org/10.1016/j.isprsjprs.2005.12.001

Wagner W., Ulrich A., Melzer T., Briese C., Kraus K. (2004). Form single-pulse to full-waveform airborne laser scanners: potential and practical challenges. International Archives of the Photogrammetry, Remote Sensing and Spatial Information Sciences XXXV-B3: 201–206.

Vain A., Yu X., Kaasalainen S., Hyyppä J. (2010). Correcting airborne laser scanning intensity data for automatic gain control effect. IEEE Geoscience and Remote Sensing Letters 7: 511–514. http://dx.doi.org/10.1109/LGRS.2010.2040578

Walter-Shea E.A., Norman J.M. (1991). Leaf optical properties. In: Myneni R.B., Ross J. (eds.). Photon-vegetation interactions - Applications in optical remote sensing and plant ecology. Springer-Verlag Berlin Heidelberg, Germany. p. 229–251. http://dx.doi.org/10.1007/978-3-642-75389-3_8

Vaughn N.R., Moskal L.M., Turnblom E.C. (2012). Tree species detection accuracies using discrete point lidar and airborne waveform lidar. Remote Sensing 4: 377–403. http://dx.doi.org/10.3390/rs4020377

Vauhkonen J., Korpela I., Maltamo M., Tokola T. (2010). Imputation of single-tree attributes using airborne laser scanning-based height, intensity, and alpha shape metrics. Remote Sensing of Environment 114: 1263–1276. http://dx.doi.org/10.1016/j.rse.2010.01.016

Vauhkonen J., Maltamo M., McRoberts R.E., Næsset E. (2014a). Introduction to forestry applications of airborne laser scanning. In: Maltamo M., Næsset E., Vauhkonen J. (eds.). Forestry applications of airborne laser scanning: Concepts and case studies. Springer, The Netherlands. p. 1–16. http://dx.doi.org/10.1007/978-94-017-8663-8_1

Vauhkonen J., Ørka H.O., Holmgren J., Dalponte M., Heinzel J., Koch B. (2014b). Tree species recognition based on airborne laser scanning and complementary data sources. In: Maltamo M., Næsset E., Vauhkonen J. (eds.). Forestry applications of airborne laser scanning: Concepts and case studies. Springer, The Netherlands. p. 135–156. http://dx.doi.org/10.1007/978-94-017-8663-8_7

Wehr A. (2009). LiDAR systems and calibration. In: Shan J., Toth C.K. (eds.). Topographic laser ranging and scanning: Principles and processing. Taylor & Francis Group, Boca Raton, FL, USA. p. 129–172.

Wehr A., Lohr U. (1999). Airborne laser scanning - an introduction and overview. ISPRS Journal of Photogrammetry and Remote Sensing 54: 68–82. http://dx.doi.org/10.1016/S0924-2716(99)00011-8

Weiss M., Baret F., Smith G.J., Jonckheere I., Coppin P. (2004). Review of methods for in situ leaf area index (LAI) determination Part II. Estimation of LAI, errors and sampling. Agricultural and Forest Meteorology 121: 37–53. http://dx.doi.org/10.1016/j.agrformet.2003.08.001

Widlowski J., Côté J., Beland M. (2014). Abstract tree crowns in 3D radiative transfer models: Impact on simulated open-canopy reflectances. Remote Sensing of Environment 142: 155–175. http://dx.doi.org/10.1016/j.rse.2013.11.016

Widlowski J.-L., Robustelli M., Disney M., Gastellu-Etchegorry J.-P., Lavergne T., Lewis P., North P.R.J., Pinty B., Thompson R., Verstraete M.M. (2008). The RAMI on-line model checker (ROMC): A web-based benchmarking facility for canopy reflectance models. Remote Sensing of Environment 112: 1144–1150. http://dx.doi.org/10.1016/j.rse.2007.07.016

Vierling L.A., Xu Y., Eitel J.U.H., Oldow J.S. (2012). Shrub characterization using terrestrial laser scanning and implications for airborne LiDAR assessment. Canadian Journal of Remote Sensing, 38: 709–722. http://dx.doi.org/10.5589/m12-057

Wu J., van Aardt J.A.N., Asner G.P. (2011). A comparison of signal deconvolution algorithms based on small-footprint LiDAR waveform simulation. IEEE Transactions on Geoscience and Remote Sensing 49: 2402–2414. http://dx.doi.org/10.1109/TGRS.2010.2103080

Wulder M.A., Coops N.C., Hudak A.T., Morsdorf F., Nelson R., Newnham G. Vastaranta M. (2013). Status and prospects for LiDAR remote sensing of forested ecosystems. Canadian Journal of Remote Sensing 39: S1–S5. http://dx.doi.org/10.5589/m13-051

Yu X., Hyyppä J., Vastaranta M., Holopainen M., Viitala R. (2011). Predicting individual tree attributes from airborne laser point clouds based on the random forests technique. ISPRS Journal of Photogrammetry and Remote Sensing 66: 28–37. http://dx.doi.org/10.1016/j.isprsjprs.2010.08.003

Yu X., Litkey P., Hyyppä J., Holopainen M., Vastaranta M. (2014). Assessment of low density full-waveform airborne laser scanning for individual tree detection and tree species classification. Forests 5: 1011–1031. http://dx.doi.org/10.3390/f5051011

146 references